THESIS FOR THE DEGREE OF DOCTOR OF PHILOSOPHY

Microstructure and liquid mass transport control in nanocomposite materials

Christoffer Karl Abrahamsson

CHALMERS
UNIVERSITY OF TECHNOLOGY

Department of Chemistry and Chemical Engineering

CHALMERS UNIVERISTY OF TECHNOLOGY

Gothenburg, Sweden 2015

Microstructure and liquid mass transport control in nanocomposite materials

Christoffer Karl Abrahamsson

ISBN: 978-91-7597-220-6

Doktorsavhandlingar vid Chalmers Tekniska Högskola

Ny Serie Nr: 3901

ISSN: 0346-718X

Department of Chemistry and Chemical Engineering

Chalmers University of Technology

Gothenburg, Sweden 2015

SE-412 96

Sweden

Telephone: +46 (0)31-772 1000

Cover image: Left part of figure; a 4.1 volume% colloidal silica gel (Bindzil 40/130) in a glass vial. Right part of figure; a simulated silica particle 3D structure, generated by a reaction limited cluster aggregation algorithm. The structure also contains a flow line visualization of the Lattice Boltzmann simulated relative flow speeds of water through the silica gel pores. The colloidal silica primary particle size is 22 nm in diameter. For more information see Paper VII.

Printed by:

Chalmers Reproservice

Gothenburg, Sweden 2015

Microstructure and liquid mass transport control in nanocomposite materials

Christoffer Karl Abrahamsson

Department of Chemistry and Chemical Engineering

Chalmers University of Technology

Abstract

Some of the biggest problems currently facing the world are closely tied to unsolved technological challenges in the material sciences. Many materials have a porous microstructure that controls their overall properties. In the case of porous materials their properties often relate to how liquids and dissolved substances move (liquid mass transport) through the pores of the material and how these substances interact with the pore walls. Challenges related to such processes can be found in applications related to energy storage, oil well engineering, food, chromatography, and drug release. It is not a trivial matter to design a material synthesis method that reproducibly produces a robust material with the correct pore-structure and surface properties and in the end, the intended function. An added difficulty is that the material should maintain its function over the intended usage period. These generic difficulties summarizes why some technological problems related to porous materials still remains unsolved. The research community is therefore trying to acquire a better understanding of the mechanisms that governs how the synthesis process affects the microstructure and the resultant liquid mass transport properties.

The focus of this work has been to investigate the nanoparticle organization in dispersions and in aggregated microporous materials, and how this organization affects the liquid diffusion and permeability through the material. To study these processes several model material synthesis methods, characterization techniques, and theoretical models were developed. Specifically the work investigated how the particle concentration, shape and aggregation conditions affected the formed microstructure. The role of microstructure anisotropy was investigated by aligning plate-shaped particles in magnetic fields during the material synthesis. In addition, the effect of several different additives on the magnetic alignment process was explored. Furthermore, a responsive nanocomposite material was synthesized in which temperature could be used to reversibly adjust the pore size of the material.

The findings showed that particle concentration, aggregation conditions, magnetic fields and temperature responsive microgels can be used to control the liquid mass transport through colloidal dispersions and gels. In some cases the experimental results together with simulations were used to derive microstructure and mass transport correlations for different particle aggregation conditions. These correlations are of general application when predicting the pore size and liquid mass transport in aggregated nanoparticle materials.

Keywords; nanocomposites, porous materials, colloidal gels, clay, silica, phase behavior, microstructure, microgels, poly(N-isopropylacrylamide), magnetic alignment, liquid mass transport, diffusion, flow, permeability, bound water, diffusion NMR, particle aggregation

List of Papers

I Magnetic alignment of nontronite nanoclay dispersions

Melanie MacGregor-Ramiasa, Christoffer Abrahamsson, Magnus Röding and Magnus Nydén

Submitted to *Applied Clay Science*

II Magnetic alignment of clay dispersions – influence of clay concentration, salt concentration and solvent properties

Christoffer Abrahamsson, Shiyu Geng, Yuman Li, Alexander Idström, Johan Bergenholtz, Michael Persson and Magnus Nydén

Submitted to *Soft Matter*

III Smart polymer-clay composite nanomaterials

Melanie Ramiasa, Katherine Locock, Christoffer Abrahamsson, Magnus Nydén

Proceedings from International Conference on Nanoscience and Nanotechnology (ICONN), 50-53, 2014

IV Magnetic orientation of nontronite clay in aqueous dispersions and its effect on water diffusion

Christoffer Abrahamsson, Lars Nordstierna, Matias Nordin, Sergey Dvinskikh, Magnus Nydén

Journal of Colloid and Interface Science, 437, 205-210, 2015

V Magnetically induced structural anisotropy in binary colloidal gels and its effect on diffusion and pressure driven permeability

Christoffer Abrahamsson, Lars Nordstierna, Johan Bergenholtz, Annika Altskär, Magnus Nydén

Soft Matter, 10, 24, 4403-4412, 2014

VI Temperature controlled liquid permeability in silica - poly(N-isopropylacrylamide) gel composites

Christoffer Abrahamsson, Hanzhu Zhang, Michael Persson and Magnus Nydén

Submitted to *Journal of Colloid and Interface Science*

VII Nanoparticle aggregation and its effect on pore size, liquid diffusion and permeability through colloidal gels

Christoffer Abrahamsson, Tobias Gebäck, Matias Nordin, Lars Nordstierna and Magnus Nydén

Submitted to *Nano Letters*

VIII Pore size effects on convective flow and diffusion through nanoporous silica gels

Charlotte Hamngren Blomqvist, Christoffer Abrahamsson, Tobias Gebäck, Annika Altskär, Ann-Marie Hermansson, Magnus Nydén, Stefan Gustafsson, Niklas Lorén, and Eva Olsson

Accepted for publication in *Colloids and Surfaces A: Physicochemical and Engineering Aspects*

Contribution Report

I	Responsible for parts of the experimental work and for writing parts of the manuscript.
II	Responsible for experimental planning and parts of the experimental work. Responsible for writing most of the manuscript.
III	Responsible for parts of the experimental planning and parts of the experimental work.
IV	Responsible for most of the experimental work and for writing most of the manuscript.
V	Responsible for most of the experimental work and for writing most of the manuscript.
VI	Responsible for experimental planning and part of experimental work. Responsible for writing the manuscript.
VII	Contributed equally much to the experimental work as Tobias Gebäck, and together we did most of the experimental work. Responsible for writing most of the manuscript.
VIII	Responsible for parts of the experimental work and for writing parts of manuscript.

List of Publications/Patents Not included in this Thesis

I Charged microcapsules for controlled release of hydrophobic actives. Part I: encapsulation methodology and interfacial properties

Markus Andersson Trojer, Ye Li, Christoffer Abrahamsson, Azmi Mohamed, Julian Eastoe, Krister Holmberg and Magnus Nydén

Soft Matter, 9, 1468-1477, 2013

II Estimation of mass thickness response of embedded aggregated silica nanospheres from high angle annular dark-field scanning transmission electron micrographs

Matias Nordin, Christoffer Abrahamsson, Charlotte Hamngren Blomqvist, Henrike Häbel, Magnus Röding, Eva Olsson, Magnus Nydén and Mats Rudemo

Journal of Microscopy, 253, 2, 166-170, 2014

III U.S. provisional patent application: "Compositions and Methods for Temperature-Controlled Permeability"

Inventors: Christoffer Abrahamsson and Michael Persson

Filed May 8, 2015

Table of Contents

CHAPTER 1

Introduction

Some of the biggest problems currently facing the world are closely tied to unsolved technological challenges in the material sciences. The development of new materials and production processes, together with a reevaluation of how we use technology, could help to handle current and future problems related to energy[1], population growth[2] and demographics[3], globalization[4] and sustainable use of resources[5, 6].

Material properties are mainly affected by the chemical composition, surface properties and microstructure of the material. Furthermore, the physical and chemical environment that surround and act on the material influence the material properties and its long term performance[7]. A number of important material groups gain their function from their porous microstructure. Examples of such porous materials can found in batteries[8], catalysts[9], diapers[10] and drug releasing implants[11], and swallowable drug tablets[12]. An important part of the function of these materials is that the pores of the material should allow for movement and interaction with gases, liquids and dissolved substances. This ability is closely tied to the materials porous structure and the surface properties of the pore walls. It is not a trivial matter to design a robust material synthesize that reproducibly produces materials with the correct pore-structure and surface properties and in the end, the intended function[13]. An added difficulty is that the material should maintain its function over the intended usage period. These generic difficulties summarize why some technological problems related to porous materials remains unsolved. The research community is therefore trying to acquire a better understanding of the mechanisms at work during the synthesis process, and their effects on the microstructure and resultant liquid mass transport properties.

Liquid mass transport in porous materials has been extensively studied in, for example, filters and membranes, and geological stone and clay formations of interest for the gas and oil industry[14], and for the retrieval or water from underground aquifers[5]. Typically these materials have a high solid volume fraction with pores in the micro- to centimeter size range[15]. Thus a

limited amount of extrapolation can be made to many of the nano- to micoporous aggregated nanoparticle systems with low solid volume fractions found in nanoparticle based materials.

Given that some of the materials studied in this thesis only consist of one type of colloidal particles, and hence are not composite materials, the name of this thesis, “Microstructure and liquid mass transport control in nanocomposite materials” could seem improper. One such example is clay particle dispersions used in this thesis. That said, clay particles are becoming increasingly important in the synthesis of nanocomposite materials. Moreover, knowledge that is acquired about, for example, liquid mass transport in pure clay dispersions should be applicable to composite clay dispersions/gels. The title of the thesis hence relates both to the findings that can applied to nanocomposite materials, as well as to actual findings made in nanocomposite materials.

In summary, this thesis aims to extend the knowledge about the aggregation-microstructure liquid mass transport relationship. Several factors that affect this relationship were explored by establishing a number of model materials, characterization techniques and microstructure or liquid mass transport models. Potential applications of the model materials are also discussed.

CHAPTER 2

What this thesis aimed to achieve

Many current problems in the material sciences would benefit from a better understanding of how to synthesize novel materials with specified microstructures. One focus of this thesis is porous materials made from colloidal particle systems, and the organization of colloidal particles in dispersions and aggregated porous microstructures. Specifically, the influence of the porous microstructure on liquid mass transport properties is of interest. The main objective is to study the aggregation-microstructure-liquid mass transport relationship in colloidal materials. It is of special interest to study the liquid mass transport in the materials under conditions where the contribution by liquid diffusion and flow to the total liquid flux is approximately equal. Under such conditions it is hypothesized that small differences in the microstructure could yield large variations in the liquid mass transport properties. This is because the flux of liquid diffusion and flow through materials scale very differently with, for example, the average pore size[16].

During the research process the thesis has also explored the optical and rheological behavior of colloidal systems in their different states. The lessons learned about liquid mass transport in colloidal materials could to some extent be generally applied to other types of nano- and microporous systems. The thesis also discuss the potential use of the model materials as liquid barriers in petroleum drilling, tunnel excavation and microfluidic applications.

The project can be divided into three parts where the first is the study of clay dispersions, gels and clay-silica composites; their phase behavior, and magnetic alignment of the clay particles in these systems **(Paper I-V)**. The objective is to study the influence of anisotropic microstructures on the liquid diffusion and flow in dilute colloidal system. A second objective is to investigate how factors, such as particle concentration and sample viscosity, affect the magnetic alignment kinetics of clay particles**.** In the second part (**Paper VI),** the objective is to synthesize a functional composite material that can be used as a liquid flow valve. The goal is to control liquid mass transport through the material by actively adjusting the transport, as triggered by temperature changes. This in turn changes the pore size, and in effect, the liquid flux through the pores. The third part **(Paper VII-VIII)** deals with the synthesis and investigation of two

types of colloidal gel systems. The microstructure, and liquid diffusion and flow through colloidal silica gels are studied using experimental characterization and computer simulations. The objective of these studies is to investigate how the particle size, particle concentration, liquid-surface interactions and aggregation conditions affect the microstructure characteristics and liquid mass transport properties in colloidal gels.

CHAPTER 3

Background

3.1 Colloidal model materials in this thesis

All the colloidal materials synthesized in this thesis filled a function as model materials to study the aggregation-microstructure-liquid mass transport relationship.

The use of model materials, as opposed to an "applied material" is motivated by several different factors, for example: (1) The cost of the material that the researcher wants to model is too high to motivate its use in experiments, (2) Some important property of the applied material is hard/impossible/expensive to characterize, (3) The applied material does not exist yet, as the model material trials is supposed to give guidance to the most suitable material design and synthesis method. In this thesis reason (2) and (3) apply. The criteria that were used to choose the model materials in this thesis were as follows:

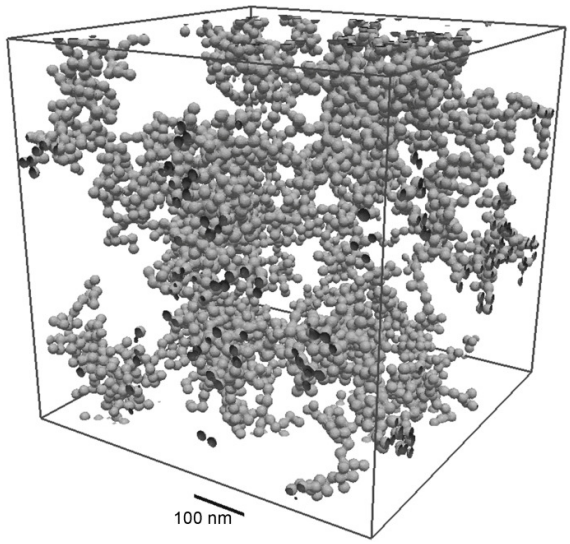

Figure 1. Aggregated particle structure generated through a reaction limited cluster aggregation algorithm (**Paper VII**). The primary particle size in 22 nm and particle concentration is 4.1 vol%.

- The synthesis of the material should be fairly straight forward and it should be possible to achieve significant differences in the microstructure by making changes to the synthesis process.

- It was of special interest to study the liquid mass transport in materials at conditions where the contributions of liquid diffusion and flow to the total liquid flux would be approximately equal. Under such conditions, the hypothesis is that small differences in the microstructure yield large variations in the liquid mass transport properties. To facilitate such

studies it should be possible to control the materials pore size and the liquid pressure over the material.

- It should be possible to image the microstructure of the material, or at least its constituents.

- It should be possible to measure the liquid mass transport through the material without the material collapsing.

- In some of the cases an additional factor of importance was if the aggregation process of the model material rendered itself to computer modeling (See Figure 1).

3.2 Clays and their magnetic responsiveness

Clays can be found in abundance all over the world and have for a long time been used by humans in applications such as housing construction and ceramics. Clays are also used in drilling fluids, foods and as barriers in nanocomposite materials, and chemical and nuclear waste containment. Clays also are known to affect slipping processes in continental plate fault zones and to cause landslides[14, 17-19].

Smectitie clays consists of crystalline plates that typically are around 1 nm thick and between 25-1000 nm wide. Smectites are known for the water absorption capability that mainly takes place in between the clay plates, in the interlayer. In a dry state the clay plates close-pack face-to-face, forming large aggregated particles. The clay plates consist of two tetrahedral layers of silica sandwiching an octahedeal layer[20] that host different multivalent metal ions such as Al^{3+}, Mg^{2+} and Fe^{3+} (Figure 2). A well known member of the smectite clay family is

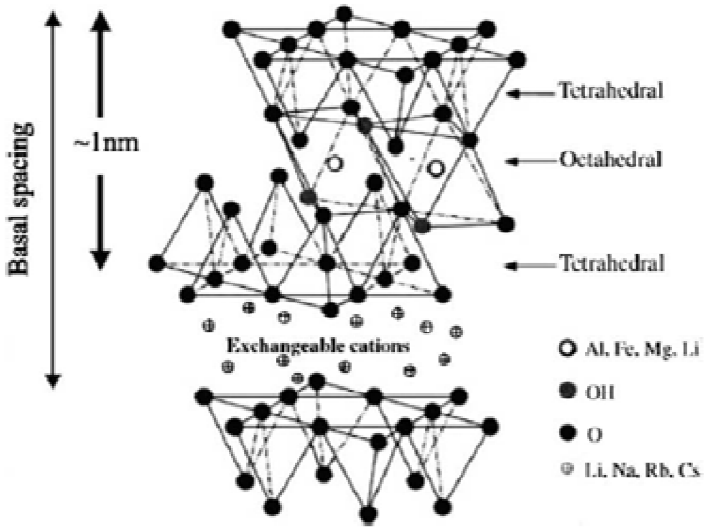

Figure 2. The smectite clay crystal structure[20] (Reprinted with permission from Elsevier, copyright 2003).

montmorillonite, however in **Paper I-V** another smectite clay mineral was used, called nontronite (Figure 3). The formula for nontronite is $(Si_{7.55}Al_{0.16}Fe_{0.29})$ $(Al_{0.34}Fe_{3.54}Mg_{0.05})$ $O_{20}(OH)_4$ $Na_{0.72}$ and the density of the nontronite as estimated from the unit-cell parameters is approximately 3.0 g/cm^3. The clay faces are negatively charged because of substitution of cations with larger charge valency, for ions with lower valences in the octahedral or tetrahedral layers of the clay crystal structure. Comparing montmorillonite and nontronite, the latter has most of its aluminium ions replaced by iron ions. To compensate the resultant negative charge of the faces, interlayer cations are present close to the clay surface. The clay plate edges, on the other hand, can sometimes be positively charged depending on the pH, as the octahedral Fe-OH or Al-OH, and tetrahedral Si-OH groups are amphoteric[21, 22](Figure 4).

The degree of magnetic responsiveness (volumetric magnetic susceptibility, χ_v) in the smectite clays is, to a large degree, a function of the iron content in the octahedral layer. For example, both the magnetic susceptibility and the iron content is eight to ten times higher in nontronite clay ($\chi_v = 4.15\times10^{-5}$) compared to montmorillonite clay ($\chi_v = 5.02\times10^{-6}$) [23].

Figure 3. Image of chunks of the clay mineral nontronite.

The magnetic properties of a material can be formulated as a Hamiltonian ($\hat{H}$) equation,

$$\hat{H} = \hat{H}_{cf} + \hat{H}_{so} + \hat{H}_{dip} + \hat{H}_{ex} + \hat{H}_z \quad \text{[Equation 1]}$$

where the terms represents the crystal field, spin-orbit, interatomic dipole-dipole, exchange interactions and the Zeeman coupling of the atomic magnetic moments to a uniform magnetic field, respectively. If a clay mineral has small amounts of iron in its structure, it often is paramagnetic and only the $\hat{H}_{cf,}$ $\hat{H}_{so}$ and $\hat{H}_z$ need to be considered.

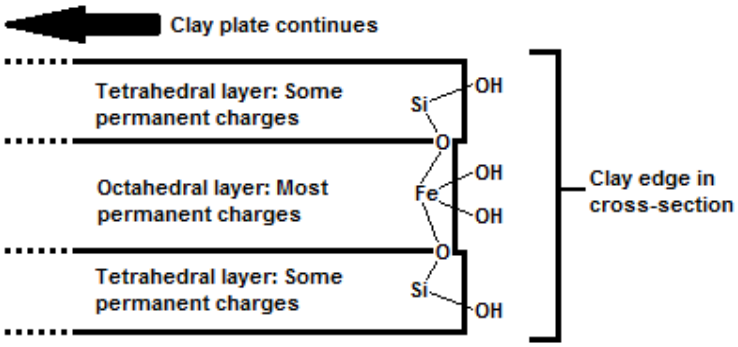

Figure 4. Schematic of the clay structure and chemistry at the plate edge. The hydroxyl groups at the edge experiences pH dependant protonation and and deprotonation.

Crystal field and spin-orbit coupling cause significant magnetocrystalline anisotropy for the Fe^{2+}, but not the Fe^{3+}. The main magnetic coupling takes place though superexchange through the Fe-O-Fe bonds. If the iron concentration is high enough the magnetic coupling can percolate, resulting in a connected exchange path throughout the entire clay plate and a strong magnetization[24].

3.3 Nontronite clay dispersions and aggregated states

Clay plates in liquid dispersions are typically stacked face-to-face in larger aggregates. If the conditions are right these clay plate aggregates can be dispersed (exfoliated) into individual plates, forming exfoliated dispersions of clays. This is commonly achieved by exchange of various ions present in the interlayer, for sodium ions that promotes exfoliation. After removing excess salt by a dialysis step the plate-plate repulsion becomes large enough for exfoliation to take place[21].

Viewed between crossed polarizers aqueous exfoliated phases of nontronite are optically isotropic at low particle concentrations, as the clay plates are randomly oriented relative to each other. However, as the clay concentration is increased the dispersions show flow birefringence,

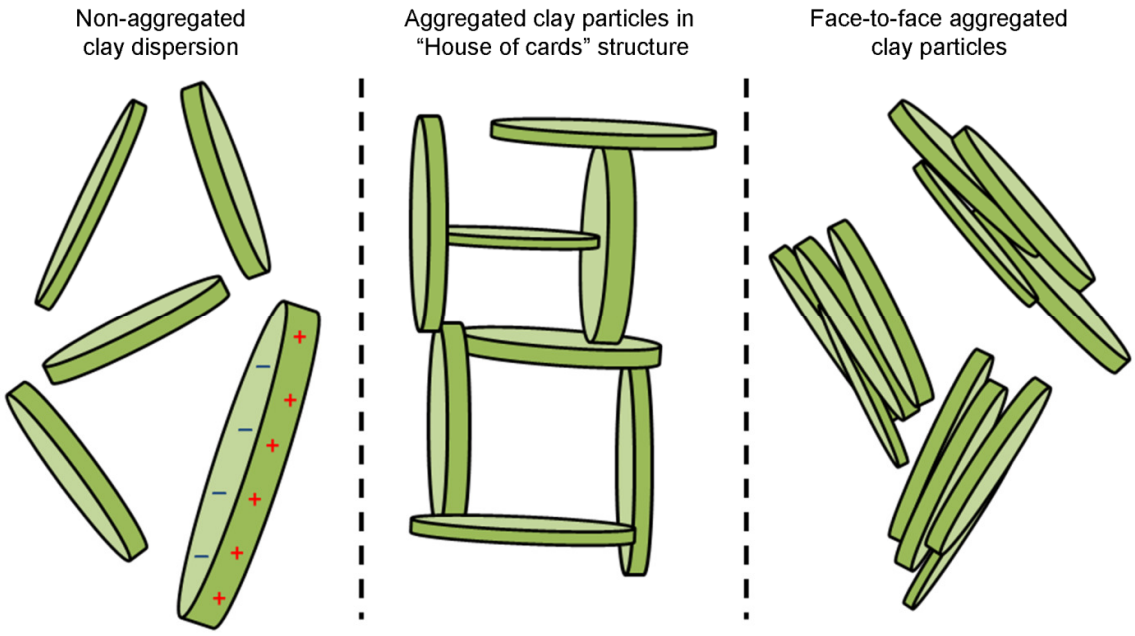

Figure 5. Schematic of different states of clay plate dispersion and aggregation. Note the marked locations of the charges on the plates. The negative charges are located on the faces of the clay plates and the positive charges on the edges.

a phenomena caused by temporary flow induced local collective orientation the of clay plates. By increasing the clay concentration further, the dispersions phase separate in some cases, forming an upper isotropic phase, and a lower birefringent nematic liquid crystal phase. Eventually the increase in clay concentration increases the volume of the lower phase until the whole sample volume is occupied by the nematic phase. In a nematic phase the clay plates have no positional order, and because of entropic forces the plates collectively orient with a long-range directional order[21]. Onsager theorized that the isotropic-nematic phase transition in anisotropically shaped colloid dispersions was entropy driven. The transition decreases the orientation entropy at the same time as entropy increases by the gain in excluded volume interactions[25].

Further increases in clay concentration result in the formation of nematic gels as the clay plates' effective volumes start to close-pack. The effective volume of a clay plate is much larger than the volume of the clay plate, and can best be represented by the ellipsoidal volume taken up by a rotating clay plate. If enough salt is added to any of the phases described above, gelation or flocculation typically occurs. Generally, low-to-moderate salt concentration results in clay gels with clay edges interacting with clay faces in a "house of cards" structure. At high salt concentration clay face-to-face attraction causes stacking of clays (Figure 5). The collective alignment of the clay plates can be observed between crossed polarizers as the dispersion shows birefringence[16].

3.4 Colloidal silica

Silica (SiO_2) is one of the most abundant minerals in the Earth's crust, where it exists both in crystalline and amorphous forms. In bulk, the silicon atoms are connected through an oxygen

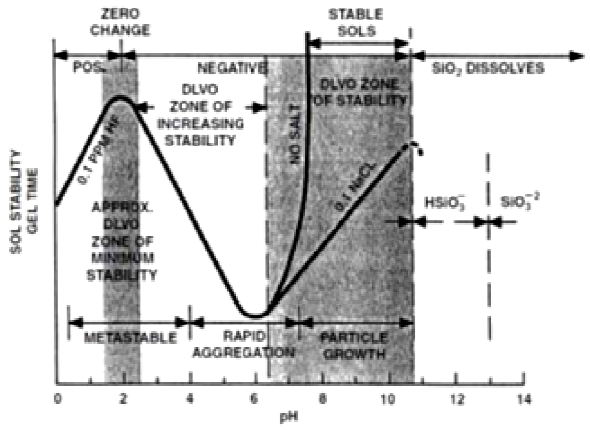

Figure 6. The effect pH and salt on the colloidal silica dispersion stability[26] (with permission from John Wiley & Sons, copyright 1979).

atom, forming a siloxane bond (-Si-O-Si-) with the silicon atom coordinating with a tetrahedral configuration. Colloidal silica that is used in **Paper V-VIII** can be synthesised from monomer forms of silica such a water glass, where pH changes or solvent evaporation can set of the nucleation growth of the nanoparticles. Dispersions with nanometer sized silica particles that do not sediment are called silica sols. In its native state the silica is covered by silanol groups (-Si-OH). Silica sols are commonly charge stabilized by deprotonation of the silanol groups at the silica surface. The deprotonation and surface charge is affected by the pH. By adding salt to the sol, the surface charges can be screened which lowers the effective repulsion between the particles. Figure 6 show the relative gel time as a function pH and the salt concentration. If the stability of the sol is lost the particles aggregate and form covalent siloxane bonds between the particles. As the aggregates grow the sol viscosity increases until the sol gels or flocculate[26].

Ostwald ripening is a phenomena that under certain conditions take place in colloidal silica gels and other colloidal systems. This process causes silica to dissolve at the convex particle surfaces of high surface energy. The dissolved silica is then redeposited on the concave surfaces of lower surface energy, for example at the neck formed at the connection point between two particles. This process typically strengthens the mechanical properties of the gel[26].

3.5 Temperature responsive polymers and microgels

Upper critical solution temperature (UCST) and lower critical solution temperature (LCST) polymers are two thermo-responsive polymer categories which solutions phase separate from a clear to an opaque state when the temperature is changed. The transition from a transparent solution to an opaque state is usually referred to as “clouding”. In both cases the polymer interaction with surrounding water is reduced, resulting in intramolecular self-association and polymer aggregates, going from a random-coil-like to a globular-like configuration[27, 28]. In **Paper III** the UCST polymer polymethacrylamide (Figure 7) is mixed with nontronite and it is hypothesised that this mixture would function as a reversible, temperature responsive fixation of the clay particles. At room temperature aqueous dispersion of polymethacrylamide is phase separated because of extensive intramolecular hydrogen bonding. If the dispersion is heated above the UCST (~50°C) the polymer experiences an increase in the solubility, with the dispersion becoming transparent. In this state the dissolved polymers would ideally allow the clay plates to freely rotate and be amendable to magnetic alignment. However, below the UCST the phase separated polymer would lock the position of the clay plates into position. In this way the orientation of the clay plates could be reversibly adjusted[29].

Poly(N-isopropylacrylamide) (PNIPAM) is one of the most well known temperature responsive polymers, with a LCST around 32°C (Figure 7)[30]. Conversely to the UCST polymer described above, PNIPAM is more soluble at lower temperatures, while it phase separates and clouds at a higher temperature. Below the LCST the amide groups of the PNIPAM polymer participate in hydrogen bonding with the surrounding water, while the hydrophobic isopropyl groups are bent to the inside of the polymer. Therefore the PNIPAM polymer has a random-coil-like configuration that binds more water below the LCST. Above the LCST the entropy causes the hydrophobic isopropyl groups to rearrange to the outside of the molecule, in which state the polymer has a compact globular-like configuration. Note that the PNIPAM is not hydrophobic above its LCST as it binds around 20-50 wt% water above the LCST. A better description could be that PNIPAM has both hydrophilic and hydrophobic properties above the LCST, however, above this temperature the phase behaviour becomes dominated by the hydrophobic properties. By adding cross-linker during the PNIPAM polymerization process temperature responsive microgels are formed[28] (Figure 8).

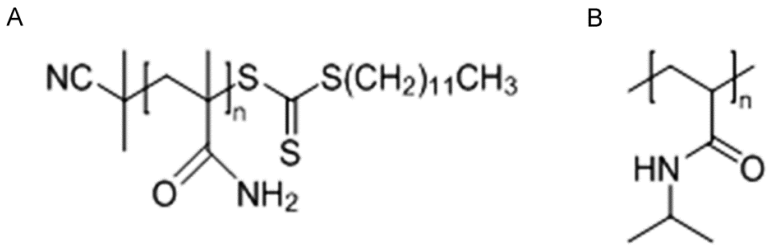

Figure 7. Molecular structure of (A) polymethacrylamide and (B) poly(N-isopropylacrylamide)

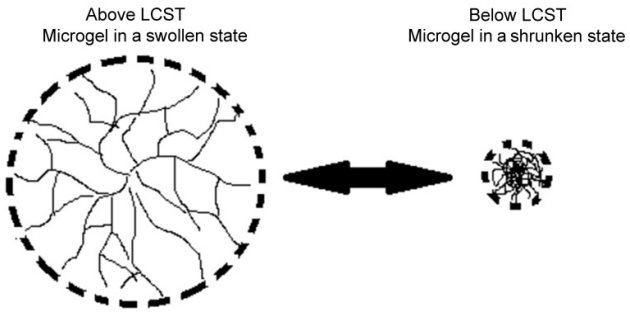

Figure 8. Schematic of the temperature induced volume change in poly(N-isopropylacrylamide) microgels.

3.6 Colloidal dispersions, aggregation and microstructures

Colloidal particles and nanoparticles are in the size range of 1-1000 nm. A liquid dispersion of such small particles that does not aggregate can be defined as a colloidal sol/dispersion. In the

dispersion the particles are defined as the dispersed phase and the liquid the continuous phase. Such dispersions are characterized by large particle surface area compared to the solid volume. Therefore the dispersion stability is largely controlled by the particle surface properties and its interaction with the continuous phase. It should be stressed that the chemical and physical properties of the particle bulk also affect the dispersion behaviour in some systems[31]. In liquid dispersions the thermal energy provides enough energy for the small colloidal particles to overcome gravity and sedimentation. Charge stabilization is a common colloidal stabilisation mechanism that result from particle surface or bulk charges that reduces the risk of aggregation by particle-particle repulsion. If the stability of the dispersions is disturbed, the particles will aggregate and flocculate, or sometimes gel[32].

The stability of a dispersion is governed by both attractive and repulsive interactions. Important attractive interactions are electrostatic forces between particles of opposite charge and Van der Waals interactions[31]. Repulsive forces include electrostatic forces between particles of the same charge, steric repulsion by for examples grafted polymers[33], or particle stabilization as present in Pickering emulsions[34]. In this thesis, electrostatic repulsion has been the dominant stabilization mechanism.

Colloidal dispersions at dynamic arrest can form gels or glasses that are non-equilibrium states of soft matter[35]. The dispersions can be destabilised by several mechanisms, such as solvent evaporation which increases the particle concentration, pH changes that can reduce the repulsive charge of the particles, and the addition of salt that causes screening of surface charges. Aggregated colloidal particle structures are often fractal-like in appearance, much like the veins of tree leaves[32]. If the particle concentration is high enough the diffusing aggregates will coalesce and form a single large aggregate that spans the whole volume of the sample, forming a gel. However, if the particle concentration is too low the aggregates are not able to span the whole volume of the sample. Instead the aggregates will sediment under the influence of gravity[35].

3.7 DLVO theory

DLVO theory (Derjaguin-Landau-Verwey-Overbeek) is often used to describe colloidal stability and interactions. The theory describes the interaction energy between two particles, taking into account attractive van der Walls interactions and repulsive electrostatic interactions of the electrical double layer, as a function of distance between the particles.

Closest to the charged particle surface there is adsorbed counter ions in a layer called the Stern layer. The electrostatic repulsion can be traced to the electric double layer that has Boltzmann distributed ions located outside of the Stern layer. In charge stabilized dispersions two charged particles that approach each other eventually have an overlap between their diffuse parts of the electric double layers. This result in osmotic repulsion between the particles, however if salt is added to the dispersion this repulsion decreases.

Figure 9 shows a typical interaction energy profile between two particles, with a deep primary minimum when the particles are close together, and a secondary minimum when they are further apart, and in-between there is an energy barrier. Typically the particles are strongly bond/aggregated in the primary minimum while the secondary minimum could host particles that are less strongly aggregated, such as loose flocculates. The addition of salt lowers the energy barrier and increases the likelihood for aggregation[26, 31].

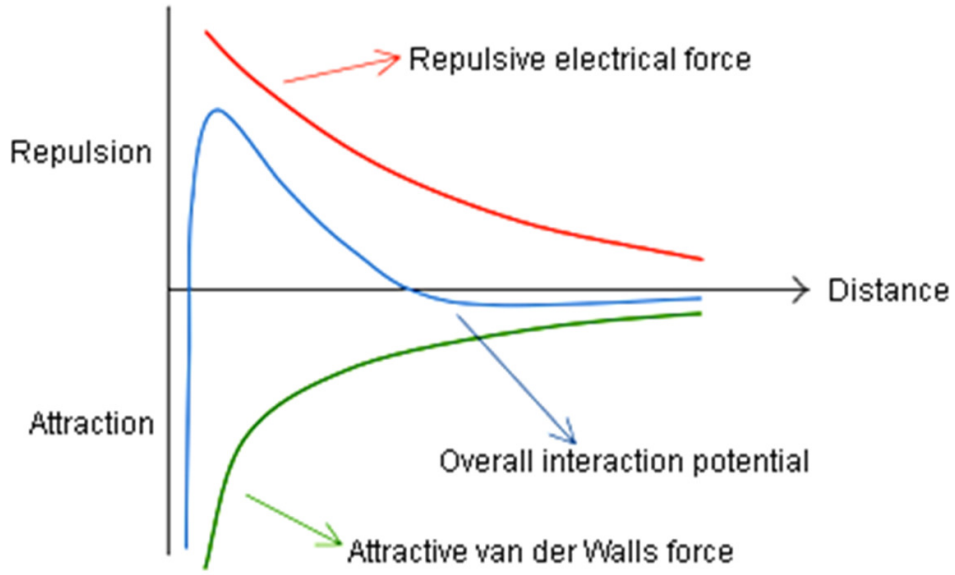

Figure 9. The interaction energy between two colloidal particles at varied interparticle distances.

3.8 The sol-gel process and porous materials

The sol-gel process is an important material synthesis processes used to synthesize, for example, silica and metal oxide particle dispersions and gels. Commonly these dispersions and gels are produced through hydrolysis and polycondensation of water glass or alkoxides[36]. In this thesis the silica starting materials for the sol-gel process were pre-formed particle dispersions. As

described above a destabilized particle dispersion can be used to make gels that consist of aggregated particle networks with liquid filled pores, or pores filled with organic precursors. In many cases the synthesized wet materials are heated up to remove any organic template present in the pores (calcined), or frozen and freeze dried, to produce a dry porous material. The sol-gel process is especially important for the production of porous materials. There are several categories of porous materials as defined by the International Union of Pure and Applied Chemistry (IUPAC). Materials with a characteristic pore size <2 nm, 2-50 nm, and above 50 nm are defined as microporous, mesoporous and macroporous, respectively. These materials have a large surface area per weight of dry material and in many cases the pore size can be tuned very precisely. Such properties are desirable in applications such as separation, catalysis, drug delivery[37].

3.9 Magnetic properties of materials

When materials are exposed to a magnetic field (H) the material acquires a magnetization (J). Figure 10 illustrates three common types of magnetic behaviours that can be observed in response to this magnetization: diamagnetism, ferromagnetism and paramagnetism. Atoms have magnetic moments originating from the orbital spin motion of electrons. The magnetic moments are quantized into units called Bohr magnetons. Quantum mechanics is necessary to fully explain the magnetic properties of solid materials, however such as description is outside the scope of this thesis.

A volume of material acquires a certain magnetization as a function of the magnetic field, Figure 10. The volume magnetic susceptibility (χ_v) is a dimensionless proportionality constant that indicates the degree of magnetization acquired per unit field,

$$\chi_v = \frac{J}{H} \qquad \text{[Equation 2]}$$

By dividing χ_v by the material density the mass magnetic susceptibility (χ_m) is found with the unit m^3/kg [38]. The magnetic susceptibility can be expected to decrease with increasing temperature according to, $\chi = 1/T$.

Diamagnetism can be found in all materials as an applied magnetic field induces a small magnetization in the material. A purely diamagnetic material has a magnetization versus magnetic field response that is linear, and a magnetic susceptibility that is negative (Figure 10A). The magnetization disappears after the magnetic field is removed. Typically atoms that

are diamagnetic have no unpaired electrons. The magnetic field changes the orbital motion of the electrons which results in a small antiparallel magnetization. Two examples of diamagnetic materials are silica [24, 39] and montmorillonite clay[23].

In ferromagnetic materials the atoms typically have unpaired electrons with magnetic moments that couple with the magnetic moments of the neighboring atoms. This produces ferromagnetism that can be orders of magnitudes stronger than paramagnetism. If a ferromagnetic material is heated from a temperature of 0 K, the material expands which increases the interatomic distances. The coupling of the magnetic moments depends strongly on the interatomic distance and the material loses its magnetic moment coupling and becomes paramagnetic if the interatomic distance becomes large enough. The temperature at which this happens is called the Curie temperature.

After an applied magnetic field is removed from the ferromagnetic material, the magnetization does not return to zero, providing a memory of the previous magnetization. The path of magnetization followed when varying the magnetic field strength experiences as hysteresis loop, Figure 10B. Examples of ferromagnetic materials are pure metallic iron, cobalt, nickel, and sometimes in combination with rare earth metals such as neodymium. Ferromagnetic materials have parallel coupling of their atomic magnetic moments. Also, they commonly have populations of atoms with opposing but unequal magnetic moments, resulting in a net magnetization. These are referred to as ferrimagnetic materials which include materials such as magnetite (Fe_3O_4) and maghemite (Fe_2O_3) [24, 39].

Paramagnetic materials also have atoms with unpaired electrons with atomic magnetic

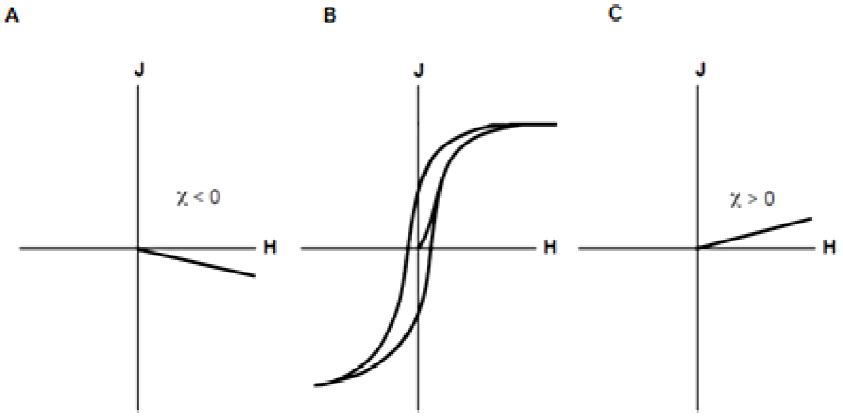

Figure 10. Magnetization (J) versus magnetizing field (H) for (A) diamagnetic substances that have a negative magnetic susceptibility. In ferromagnetic substances the (B) path of magnetization versus magnetizing field shows hysteresis and the magnetic susceptibility cannot be represented by a constant. (**C**) paramagnetic substances that have a positive magnetic susceptibility.

moments. Paramagnetic materials experience a linear magnetization as function of the magnetic field strength and have a positive magnetic susceptibility (Figure 10C). Conversely to ferromagnetic materials the magnetic moments do not couple with neighboring atomic magnetic moments which gives a weaker magnetic response. If a paramagnetic material is aligned in a magnetic field and the field is removed, the magnetic moments are randomized due to the thermal energy inside the material, resulting in lost magnetization. One example of a paramagnetic material is nontronite clay[24, 39].

3.10 Magnetic alignment of fiber/plate particles in a viscous medium

The dynamic behavior of clay plates as a function of magnetic field strength can be estimated by an equation that was previously developed to describe the magnetic orientation of a fiber dispersed in a liquid viscous medium[23, 40]. The analogy to fibers could work especially well for nontronite clay that consists of lath shaped (rectangular) plates. Magnetic alignment of dilute clay plate dispersions can be described by the balance between the magnetic and hydrodynamic torque,

$$L\frac{d\theta}{dt} = \frac{1}{2}V\chi_a \mu_0 H^2 \sin 2\theta \qquad \text{[Equation 3]}$$

The right side of Equation 3 represents the magnetic torque, where V is the volume of the fiber, χ_a the volume anisotropic diamagnetic susceptibility, μ_0 the magnetic permeability of vacuum, and H the magnetic field. Note that the magnetic torque depends on the clay plate volume, but not on the shape of the plates. The left side of the equation describes the hydrodynamic torque that the viscous medium exerts on the plate when it rotates with an angular velocity ($d\theta/dt$), where θ is the angle between H and the largest sheets axis, t is time. L is dependent on both the clay plate volume and shape. Solving Equation 3 results in,

$$\tan\theta = \tan\theta_0 \exp(-t/\tau) \qquad \text{[Equation 4]}$$

where the alignment rate $|\tau_a^{-1}|$ is defined as,

$$\tau_a^{-1} = (V/L)\,\chi_a \mu_0 H^2 \qquad \text{[Equation 5]}$$

For a sphere with radius a, $L = 8\pi\eta\, a^3$ and $V = (4/3)\,\pi\, a^3$ Equation 5 becomes,

$$\tau_a^{-1} = \chi_a \mu_0 H^2/6\eta \qquad \text{[Equation 6]}$$

where η is the viscosity of the medium. If $\chi_a > 0$ the angle θ decreases until the particle aligns parallel with the magnetic field. Conversely, if $\chi_a < 0$, the angle increases until it reaches perpendicular alignment.

A general formula for the hydrodynamic torque acting on an ellipsoid rotating in a viscous medium is,

$$L = 8\pi\eta a^3/F(D) \qquad \text{[Equation 7]}$$

with the shape function,

$$F(D) = \frac{3D\left(-2D\sqrt{D^2-1}+\left(1-2D^2\right)\ln\frac{D-\sqrt{D^2-1}}{D+\sqrt{D^2-1}}\right)}{4\left(D^2-1\right)\left(D^2+1\right)\sqrt{D^2-1}} \qquad \text{[Equation 8]}$$

where 2a is the length of the plate's short axis and D is the aspect ratio. With $V=(4/3)\pi a^3 D$ for the ellipsoid, we obtain,

$$\tau_a^{-1} = \frac{F(D)\chi_a\mu_0 H^2}{6\eta} \qquad \text{[Equation 9]}$$

or if rewritten in terms of magnetic flux density(B),

$$\tau_a^{-1} = \frac{F(D)\chi_a B^2}{6\eta} \qquad \text{[Equation 10]}$$

3.11 Brownian relaxation of particles in a viscous medium

Aurish and colleagues have described the relaxation rate $|\tau_r^{-1}|$ for non-interacting particles that are dispersed in a viscous liquid after they have been fully aligned in a magnetic field[41]. They used the following equation,

$$\tau_r^{-1} = k_B T/3\eta V_{hyd} \qquad \text{[Equation 11]}$$

where η is the viscosity, V_{hyd} the hydrodynamic volume of the particle, k_B the Boltzmans constant, and T the temperature.

3.12 Liquid mass transport in microporous materials

Within the geosciences, pressure induced permeability have been studied in purified clay minerals and clay soils[42, 43]. From these investigations it is clear that the salt concentration have a large impact on the structure and permeability of clay dispersion and gels. Generally, low-to-medium salt concentration result in clay gels that adopt a "house of cards" structure, with the clay edges interacting with clay faces, while at higher salt concentrations the faces of the clays can attract each other. Clay face-to-face attraction causes stacking of clays, forming larger particles and in effect larger pores between the particles and higher permeability. Similarly, the presence of moderate salt levels have been theorized to reduce the interaction between the water moving though pores and the clay surfaces, increasing the mobility of the water through the pores. The effect of clay orientation on mass transport properties such as diffusion has been the target of several studies in both pure clay dispersions and clay composites[19, 44, 45]. Moreover, gas permeability in clay composites was studied by DeRocher and co-workers and they found that the permeability decreased noticeably when the clay particles were oriented perpendicular to the mass transport flux, which was the only clay orientation they investigated[46]. Huang et al. compared the ion-conductivity, a property that have similarities to fluid permeability, between samples with oriented or non oriented clays in polymer electrolytes at low clay volume fractions and found that orientation of clays parallel to the direction of electron flux increased ion-conductivity of the material[47].

In soil and rock, the connectivity of the pore space can be an important mass transport parameter as a poor connectivity can make large parts of the material non-conductive to mass transport. Compared to such, the materials studied in this thesis have much lower volume fraction of material. Therefore the connectivity of the material pores, as experienced by the solvent, can be assumed to be very high. However, when larger particles or molecules moves though colloidal gels they can be restricted when their size gets close to the average pore size of the gel network[48] .

CHAPTER 4

Materials and methods

4.1 Particle synthesis methods

Exfoliated clay dispersions were prepared by ion exchange of the clay interlayer ions by sodium ions, were the latter promoted exfoliation of the clay plates. The clay dispersions were then size fractionated by ultracentrifugation. In short, naturally occurring nontronite mineral was ground to a powder and dispersed in a 1M NaCl solution. The dispersion was ultrasonicated to aid the breakup of the clay powder. The dispersion was centrifuged at 35000×g for 90 min and the sediment was redispersed in new NaCl solution. The centrifugation and redisperion were repeated in total three times. This process ion exchanged any ions present in the interlayer of the clay aggregates for sodium ions. During the following dialysis excess ions were removed which reduced the screening of clay surface electrostatics. The increased clay-clay particle repulsion allowed for exfoliation. The redispersed sediment was sorted by plate size though ultracentrifugation size fractioning at 7000×g, followed by 17000×g (Fraction 2). The fraction 2 sediment was a transparent green-yellow highly viscous liquid-gel that was reconstituted to form the samples used in all experiments.

The PNIPAM microgel synthesis was performed by free radical polymerisation of N-isopropylacrylamide and methylenebisacrylamide cross-linker in nitrogen purged aqueous solutions. Ammonium persulfate was added to initiate the reaction. The reaction mixture was magnetically stirred for 4 hours at 70°C, cooled to room temperature and then dialysed against deionized water until there was no change in conductivity. The dialyzed PNIPAM microgel dispersion was concentrated by ultracentrifugation at 14000 RPM for 2.5 hours, yielding a 6.0 wt% PNIPAM sediment that was used to make the silica-PNIPAM composite gels.

The silica sols (Bindzil 40/130 or 50/80), consisting of 40-50 wt% aqueous dispersions of nano-sized silica spheres, were kindly provided by AkzoNobel Pulp and Performance Chemicals, Sweden.

4.2 Sol-gel sample synthesis

Direct addition of salt to clay dispersions result in instant gelation in some parts of the samples, because of uneven salt distribution. Moreover, a mixing partly gelled dispersion yields an inhomogeneous sample consisting of gel lumps[16]. Direct addition of salt to a clay solution do not allow for magnetic clay alignment, at least a higher salt concentrations, as the clay particles aggregate and are locked into position before alignment can take place. In **Paper II** and **V** this problem was avoided by gradually increasing the salt concentration by *in-situ* generation of salt. This allows time for magnetic clay alignment before the salt concentration becomes high enough to gel the dispersion. *In-situ* generation of salt was achieved by first mixing the colloidal particle sol of interest with urea solution, followed by addition of a smaller amount of urease enzyme solution (Sigma, Jack Bean-urease type IX, Specific activity ~75,000 U/g). The enzyme hydrolyses the evenly distributed urea to ammonia. This increases the pH to the reaction buffering pH of 9.2, after which ammonium bicarbonate is generated. The reaction progresses according to the formula,

$$NH_2CONH_2 + H_2O \xrightarrow{\text{urease}} CO_2^{2-} + 2NH_4^+$$

As the salt concentration is increased homogenously and gradually throughout the whole sample volume, no mixing is needed to distribute the salt evenly. At an initial urea concentration of 1 M, the gelation of a clay dispersion typically take place 10-20 minutes after enzyme addition.

In **Paper VI-VIII** direct addition of salt solution could be used as the dispersions did not contain clay. In some of the studies the silica sol pH was adjusted to 7.0-7.8 by ion exchange and filtered with a syringe filter to remove any larger aggregates. Samples were prepared by vortexing a mixture of filtered silica dispersion, NaCl solution and double distilled water and letting the samples to gel undisturbed for one week. A 9 wt% silica dispersion with a 1 M NaCl concentration typically gelled 2 hours after salt addition.

4.3 Crossed polarizer and birefringence

The presence of optical birefringence in a material can be visualized by viewing it between two crossed polarizers. In colloidal materials the birefringence is commonly produced by regions of the dispersion/material with an anisotropic microstructure. Optical polarizers act as optical filters (Figure 11) that only lets through light that is linearly polarized in one direction. By placing a second polarizer with its slits oriented perpendicularly to the first polarizer, all incoming light will be extinguished. However, if an optically transparent sample with an

anisotropic microstructure is placed between the polarisers, the linearly polarized light will be refracted at an angle in the sample so that part of the light can exit the second polarizer. The alignment axis of the microstructure in a region of the sample can be found by rotating the crossed polarizers until that particular region of the sample appears dark; the microstructure alignment axis of that region is then parallel with the slit grating of the first polarizers. The strength of the birefringence can with the right controls be used to estimate the degree of microstructure alignment. In isotropic dispersions light is refracted at a constant angle, passing through it at a single velocity without being polarized. However, in dispersions with anisotropic microstructure the light is double refracted into two rays with different directions and velocities, relative the polarization axis of the microstructure[49].

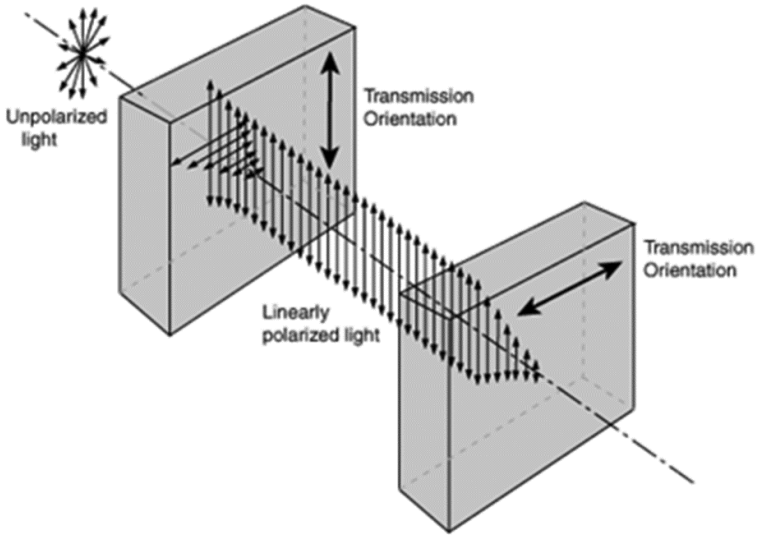

Figure 11. Schematic illustrating the effect of crossed polarizers on unpolarized light. No light exits through the second polarizer as the polarizer's slit directions are set perpendicular to each other[49] (with permission from Dr. Rod Nave, HyperPhysics Project, copyright 1979).

4.4 NMR diffusion measurements and diffusion

Diffusion NMR uses magnetic field gradients to follow the physical location of diffusing species in solution along the direction of an applied field gradient, which is normally the z-axis of conventional NMR probe heads. In that way the diffusion coefficient of the diffusing species can be obtained. Compared to other techniques that are used to measure the diffusion coefficient, diffusion NMR have a number of benefits, as it allows for relatively fast measurements without needing to use tracer diffusants such as radioactive species. Instead the diffusion of species that are normally in the system can be used as tracer molecules, such as water in hydrogels[50]. Diffusion NMR measures the self-diffusion coefficient, D_{self}, of the

Brownian translational motion of diffusing species. Even though the average displacement of a molecule in an isotropic 3D-system is zero, the mean square displacement is not zero. In fact the distance a molecule moves over time (t) in a particular direction can be described by

$$z_{rms} = \sqrt{2D_{self}t} \qquad \text{[Equation 12]}$$

where z_{rms} is the root mean displacement average over time for a population of molecules. The self-diffusion coefficient will be affected by the size, shape and physicochemical properties of the diffusing species, as well as the solvent properties and the system temperature. In porous materials additional aspects such as microstructure and the interaction between the diffusing species and the pore walls need to be considered.

The molecular mobility (ν) have an inverse relationship with the friction coefficient (*f*), $\nu = f^{-1}$. The diffusion drag depends to a large extent on the size and shape of the diffusing species. Moreover, D_{self} can be related to the Einstein relation $D_{self} = k_B T\nu$, where k_B is the Boltzmann constant and T the absolute temperature.

The viscous drag in a liquid on diffusing species with spherical shape can be estimated by stokes law:

$$f = 6\pi\eta r \qquad \text{[Equation 13]}$$

where η is the viscosity of the liquid and r the hydrodynamic radius of the sphere. The relation between the size of the diffusing species and the self diffusion can be described by the Stokes-Einstein law[51].

$$D_{self} = \frac{k_B T}{6\pi\eta r} \qquad \text{[Equation 14]}$$

Most NMR measurements in this thesis have been performed on a Bruker Avance 600 spectrometer (Bruker, Karlsruhe, Germany) with a diffusion probe with a maximum gradient strength of 1200 G/cm and with a 5 mm RF insert with 1H and 2H coils.

4.5 Permeability measurements

To measure the permeability of the gelled materials the flow speed over the material at a certain pressure was measured. This was done by casting the gel-plug of interest at one end of an open-ended tube. The tube and gel plug together forms the column. Such columns were constructed from glass tubes, for example, in one configuration the bottom of a 5-mm-diameter glass NMR tube was removed. To support the gel plug, a 210-micron polyester mesh was glued to one of

the openings (Figure 12). The same tube end was then sealed with parafilm and the column was filled with sample mixture up to 30 mm from the mesh, and the other end was sealed with parafilm. After letting the gel-plugs gel at rest for 1 week, the parafilm was removed and the columns were fixed upright in a stand over a beaker filled with 0.5 or 0.9M NaCl and magnetic stirring. The columns were filled with 90 mm of 0.5 or 0.9 M NaCl solution on top of the gel plug, effectively creating a pressure gradient over the material. In the beaker, the NaCl solution level was adjusted to match the top of the gel plugs. The top position of the NaCl solution in the columns was monitored 2 times a day for at least 3 days by marking the columns with a marker pen.

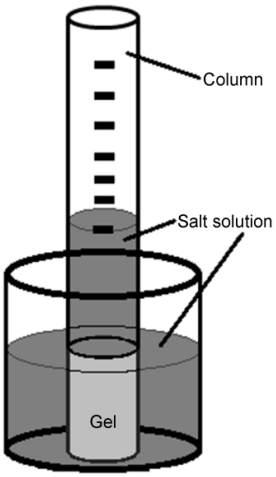

Figure 12. Schematic of setup used for liquid permeability measurement (not drawn to scale). The flow speed of the salt solution through the gel-plug is followed over time by marking the tube with a marker pen at the top position of the salt solution.

The flow speed was close to linear for the first week in all samples, and the results were used to calculate the liquid permeability using Darcy's law:

$$v_f = \frac{\kappa}{\mu}\frac{\Delta P}{\Delta z} \qquad \text{[Equation 15]}$$

In Equation 15, v_f is the flow speed of the liquid through the gel, κ (m^2) is the permeability of the gel, μ is the dynamic viscosity of the salt solution, ΔP is the pressure applied over the gel and Δz (m) the gel thickness[16].

4.6 TEM and sample preparation

The particle microstructures of the gels in this thesis were most of the time visualized with transmission electron microscopy (TEM). TEM is a common technique to visualise material microstructures. The technique can only image thin samples as the electrons need to be transmitted through the sample and onto a fluorescent screen or digital detector to obtain a micrograph. Areas of the sample with more material or atoms of higher atomic number will give more contrast in TEM and appear darker. TEM is one of the most powerful techniques when imaging small material features, with a resolution down to a few Ångstroms. As samples are imaged in vacuum in TEM, all water needed to be removed from the colloidal gels. In addition, the samples need to be mechanically reinforced to withstand the microtoming into thin slices. Both these demands can be achieved by embedding the gels in a polymer resin[52]. The water in the gels was first exchanged with increasing ethanol concentrations followed by resin in ethanol. Polymerization of resin took place at 60 °C and ultrathin sections ~60 nm were cut with a diamond knife using an ultramicrotome. The thin sections were placed on copper grids and imaged in a TEM of model LEO 906E made in LEO Electron Microscopy Ltd., Oberkochen, Germany.

The use of TEM to image bio- or petroleum-based polymers can be complicated. This is partly because carbon based compounds show both low electron contrast in TEM, as well as sensitivity to electron beam damage. Low accelerating voltages can reduce the problem of beam damage, but it also reduces the micrograph resolution. Often time-consuming sample preparation processes are needed to stain the microstructure with atoms of high atomic mass that give higher electron contrast. Another problem is that the native structure of the material can be disturbed by the staining, and/or the dehydration of the material that is necessary for the high vacuum condition used in TEM[52].

Colloidal silica and clay have been shown to have good contrast in TEM, and silica or silica-clay composites forms gels that can be resin embedded.

CHAPTER 5

Results and Discussion

The results and discussion section of the thesis focuses on how particle aggregation affects the microstructure, and the liquid mass transport in colloidal gels. The results are discussed in the following order. First the studies involving clay are discussed, followed by the colloidal silica with PNIPAM microgels composites, and finally the studies treating colloidal silica by itself.

5.1 Phase behavior, microstructure and magnetic alignment in clay dispersions and gels

This section starts out by discussing the appearance and phase behavior of clay dispersions as a function of particle, salt and glycerol concentration, and UCST-polymer concentration. Thereafter follows a discussion about how these factors control the magnetic alignment of the clay particles.

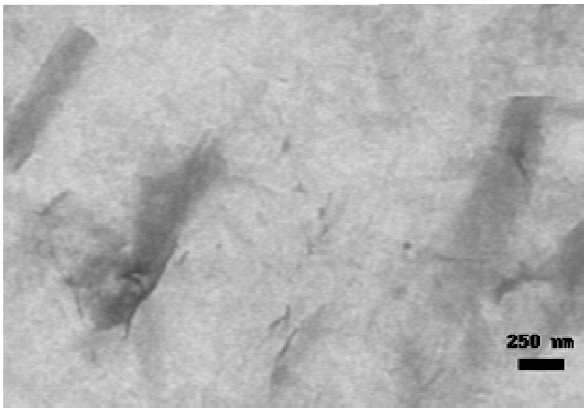

Figure 13. TEM micrograph of nontronite plates seen as dark plate-shaped shadows in the micrograph.

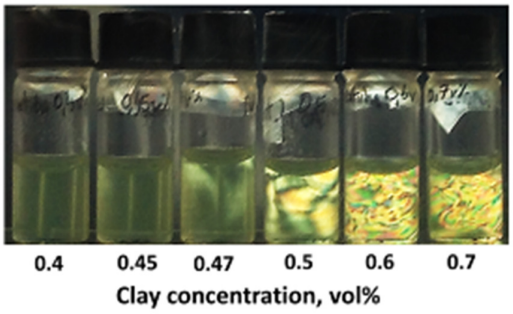

Figure 14. Nontronite dispersions phase behavior (fraction 2) observed in between crossed polarizers as a function of increasing clay concentration.

5.2 Nontronite dispersions and composites

In **Paper I-V** exfoliated nontronite dispersions that consisted of dispersed lath shaped clay plates were prepared (Figure 13). Clay plates of different sizes were separated into different fractions by centrifugation. Typically the size fraction used in the experiments had a plate

length in the range of 200-400 nm. The thickness of the nontronite plates has been estimated to 0.7 nm in earlier studies[21].

The optical phase behavior of the pure nontronite dispersions (only nontronite and water) was investigated between crossed polarizers as this gives information about the particle-particle arrangement in the dispersions (Figure 14). In all studies the nontronite dispersions have been optically isotropic at low clay concentration, and birefringent as the nontronite concentration increased. The birefringence indicates the presence of local regions of collective clay plate alignment. Isotropic dispersions of higher clay concentration have showed flow birefringence after shaking that relaxed within seconds to days.

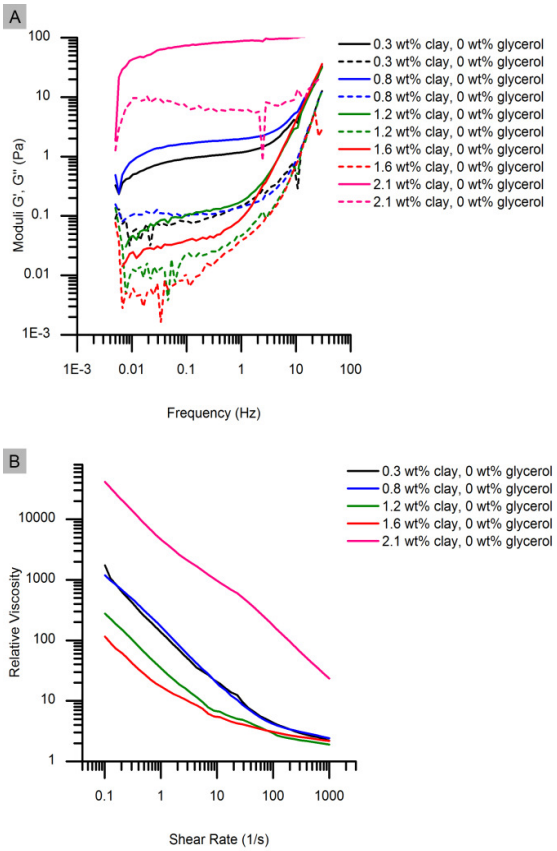

Figure 15. Rotational rheometer results for pure clay dispersions. (A) Frequency sweep for samples with no glycerol and different clay concentrations, the range of frequency is from 0.5 Hz to 30 Hz. (B) Second time ascending and descending flows for samples with no glycerol and different clay concentrations, the shear rate is from 0.1 to 1000 s^{-1}.

In **Paper II** phase separation were observed in clay dispersions that had a set NaCl concentration of 10^{-4}M, with a clay concentration that were close to the gelation point. The lower phase was birefringent and the upper phase isotropic, indicating the formation of a lower nematic-like phase. To conclusively say that the phase is nematic small angle x-ray measurements (SAXS) would be needed. Nematic phase separation has previously been reported for nontronite from another source in the presence of 10^{-4}-10^{-3} M NaCl[21]. No phase separation was observed in the nontronite clay dispersions in **Paper I, III** and **V**, which had higher or lower salt concentration than **Paper II**, or a different type of salt. Thus just the right concentration of NaCl is needed to induce nematic-like phase separation as this provides just the right amount of screening for the

nontronite phase behavior to be dominated by entropic interactions[25]. Higher clay concentrations do not allow for nematic-like phase formation because of aggregation events.

In **Paper I** the viscosity increased significantly at high clay concentration as judged by an inverted tube test. The dispersions with a clay concentration around 0.6-0.7 vol% appeared to be gels. This is in line with what have been previously reported for nontronite dispersions of similar composition[53]. The sol-gel transition was estimated by excluded volume theory[53]. Using the experimentally determined average clay plate dimensions, the theory predicts a sol-gel transition at 0.3 vol% which is close to the experimentally estimated sol-gel transition. The difference between prediction and experiment was attributed to factors that are not considered in the model, such as clay plate size polydispersity and electrostatic particle-particle interactions[21].

The pure clay dispersions in Figure 15 shows a re-entrant storage (G') and elastic G'' moduli, and relative viscosity at an increasing clay concentration in **Paper II**. All these properties have a minimum at a clay concentration of 1.6 wt%. The relative viscosity is the viscosity of the clay-glycerol dispersion normalized to the pure glycerol solution of the same glycerol concentration. Michot and coworkers also observed a re-entrant behavior as function of clay concentration in nontronite dispersions from another source, using the same set salt concentration (10^{-4} M NaCl)[54]. The re-entrant behavior at increasing clay concentrations can be attributed to nematic-like phase transitions and aggregation events as follows. Under some conditions, isotropic clay dispersions are reported to be more viscous than nematic ones due to the possibility of collective particle movement in nematic phases. However several phase separated samples in **Paper II** showed a lower non-birefringent phase that is unlikely to be nematic (See Supportive information **Paper II**). This suggests that the reentrant rheological behavior could be associated with loose flocculate formation with a house of cards structure in these samples. Such phase separated non-birefringent phases have for example been observed in hectorite clay dispersions[55].

5.3 Clay dispersions with added glycerol and salt

The effect of clay, glycerol and salt concentration on the nontronite dispersion phase behavior and the magnetic clay alignment kinetics were studied in **Paper II**. Figure 16 shows clay dispersions viewed between crossed polarizers with different clay and glycerol concentrations. At a fixed temperature aqueous glycerol solutions without clay becomes more viscous with higher glycerol concentration, potentially allowing for the viscosity of the solution to be tuned several orders of magnitude[56]. The dispersions were optically isotropic or birefringent and some of the dispersions with 1.2 wt% clay, with and without glycerol, were also phase separated after 60 days, but the lower phase was not birefringent. Moreover, the volume of the lower phase increased at higher clay concentrations. The lower phase in some of the phase separated samples was not birefringent. As mentioned above, this is because the lower phase most likely is a loose flocculate made up of edge to face aggregated clay sheets of isotropic orientation (Figure 5). In

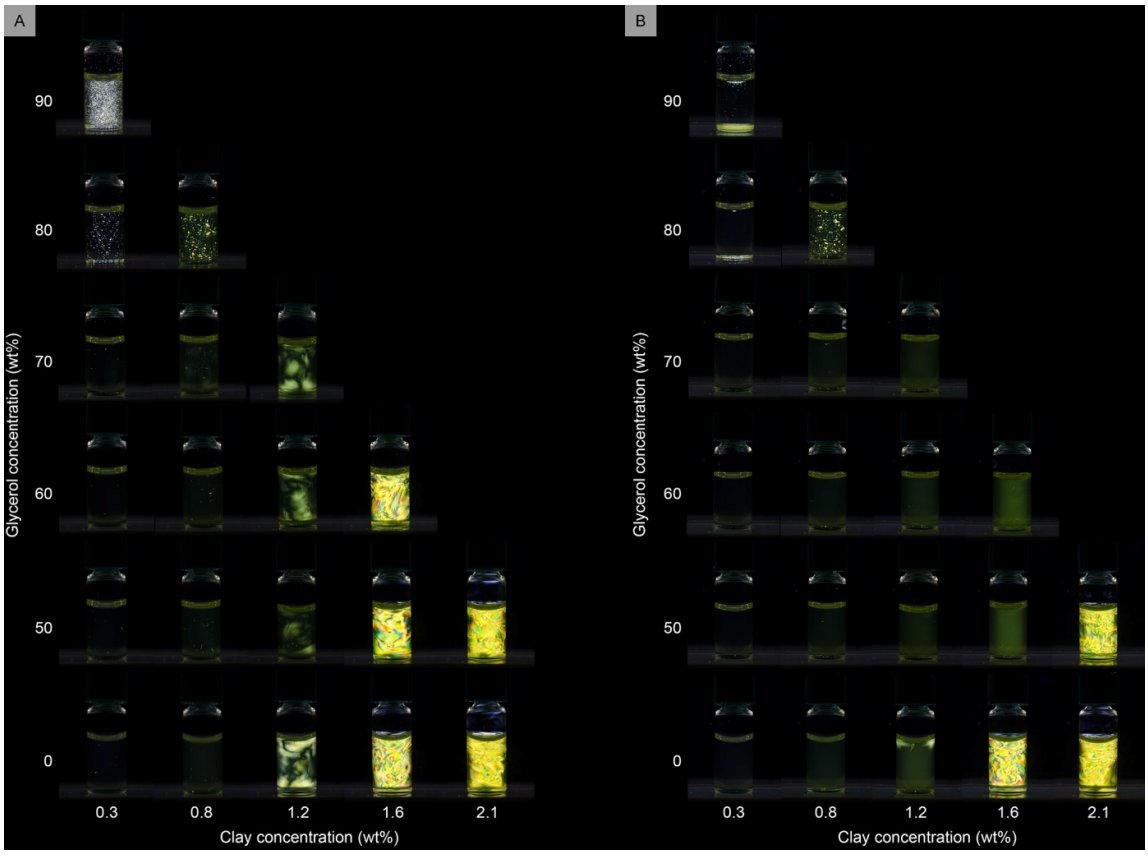

Figure 16. Nontronite clay-glycerol dispersions imaged between crossed polarizers (A) directly after shaking the vials, and (B) after being left undisturbed for 5 days. The salt concentration in all samples was set to 10^{-4} M NaCl.

Figure 16 the dispersions with high glycerol concentration (80 - 90 wt%) were initially homogenous. After a few days macroscopic particles formed that sedimented over time. The dense particles in the dispersion with 0.8 wt% clay and 80 wt% glycerol were still suspended in the whole liquid volume because of the increased viscosity and reduced sedimentation speed in the dispersions with a clay concentration of 0.8 wt% compared to 0.3 wt% clay.

In Figure 17 an increase in glycerol concentration from 0 to 50 wt% resulted in a shorter birefringence relaxation time at 1.2 wt% clay. In both 1.2 and 1.6 wt% clay dispersions a glycerol concentration increase from 50 wt% and upwards increased the relaxation time sharply. Figure 17A illustrate that dispersions with 1.6 wt% clay have longer relaxation time than the 1.2 wt% clay dispersions. Similarly, samples with 60 wt% glycerol need longer time to relax than samples with 50 wt% glycerol. The birefringence relaxation kinetics are consistent with the qualitative observations in the phase diagrams in Figure 16.

The macroscopic particle formation at high glycerol concentration in Figure 16 suggests face-to-face aggregation of the clay plates at high glycerol concentration. The aggregation could be induced by glycerol's comparably lower dielectric constant, that is roughly half that of water. This suggest that glycerol reduces the clay plate particle-particle repulsion[57]. Michot and colleagues observed formation of sediment particles in nontronite dispersions with 10^{-2} M NaCl suggesting that the glycerol affect the colloidal stability similarly to salt, although considerably less salt compared to glycerol is need to induce destabilization[54]. Glycerol is currently used as an additive in oil well drilling fluid were it has been shown to efficiently reduce the water uptake and swelling in smectite clay rich geological formations. This is in

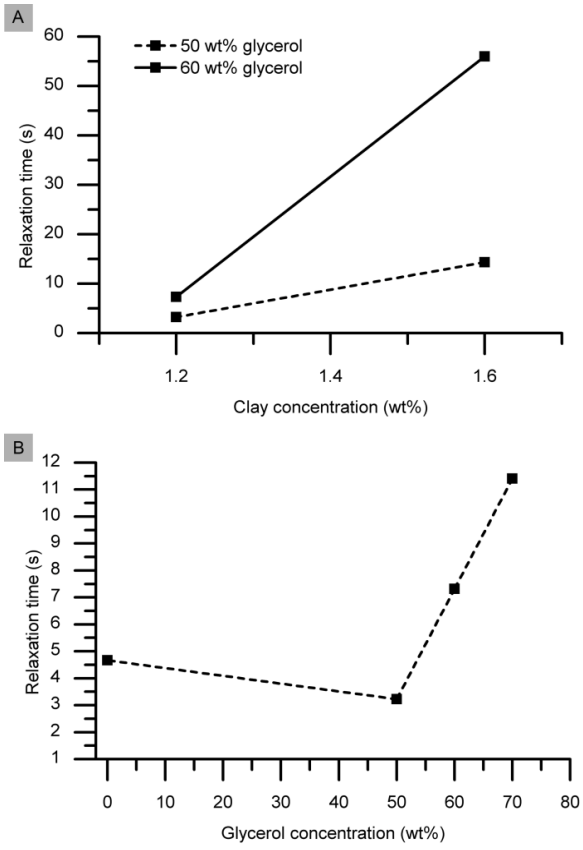

Figure 17. The birefringence relaxation time in (A) dispersions with different clay and glycerol concentrations, and (B) dispersions with 1.2 wt% clay with different glycerol concentrations.

certain situations preferable as swelling clay deposits in the drill hole can result in problems such as drill jamming during operation[58].

5.4 UCST polymer addition

The UCST polymer polymethacrylamide with an UCST ~50°C was added to nontronite dispersions to achieve reversible and heat triggerable immobilization of the clay plates (**Paper III**). In Figure 18 clay dispersions with and without 1.0 wt% UCST polymer are viewed between crossed polarizers. The addition of the UCST polymer shifts the isotropic to birefringent transition to a higher clay concentration. Thus the polymer impedes the formation of nematic-like phases. An interesting observation was that a dispersion with 0.8 vol% clay and 1.0 wt% UCST polymer acted as a gel in an inverted tube test at room temperature, while it flowed as a dispersion when heated to 50°C. The results suggest that the dispersions can be reversible gelled by varying the temperature, however, the gelation does not seem to efficiently lock the clay into place as all samples aligned in a magnetic field.

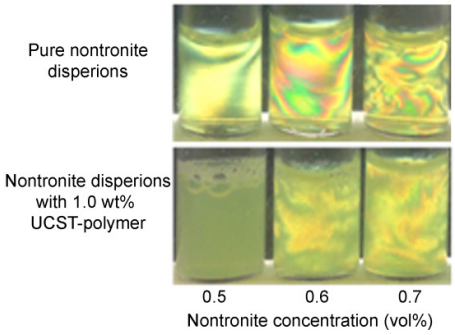

Figure 18. Clay dispersions at varied clay concentration viewed directly after vortexing between crossed polarizers, without and with the UCST-polymer polymethacrylamide (1.0 wt%). Note the reduced birefringence in the presence of the UCST polymer.

5.5 Magnetic alignment of pure and mixed clay dispersions

In Figure 19 and 20 the effect of clay concentration and magnetic field strength on the optical birefringence is illustrated (**Paper I-III**). Dispersions containing between 0.3 and 0.5 vol% of clays were birefringent, even in 0.25 T, and the glow intensity increased with the magnetic field strength and clay concentration. No birefringence was observed below 0.2 vol%, and the sample with 0.2 vol% clay was only birefringent in the strongest magnetic field, 0.81 T. Assuming that the birefringence intensity correlates with the degree of plate alignment, these results support two hypotheses proposed by experts in the field[59]: 1) stronger magnetic fields induce higher ordering of the clays and 2) long-range collective ordering results in higher degree of alignment in concentrated dispersions. In other words, the

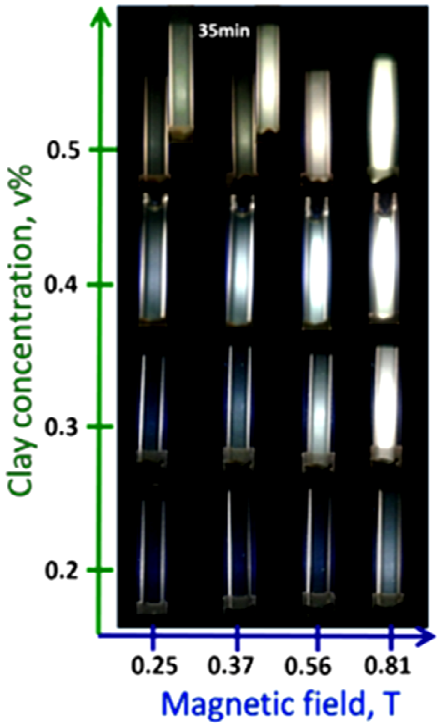

Figure 19. Glass capillaries filled with nontronite dispersions observed between crossed polarizers after 1 min exposure to the magnetic field. The images of the top two samples (0.5 vol%) are obtained after 35 min exposure to 0.25 and 0.37 T.

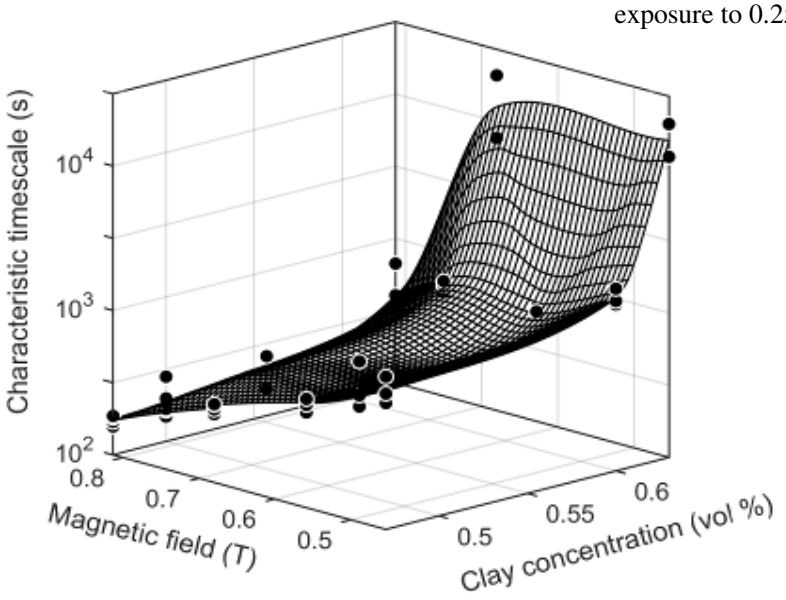

Figure 20. Characteristic times for clay alignment as a function of the clay concentration and magnetic field strength.

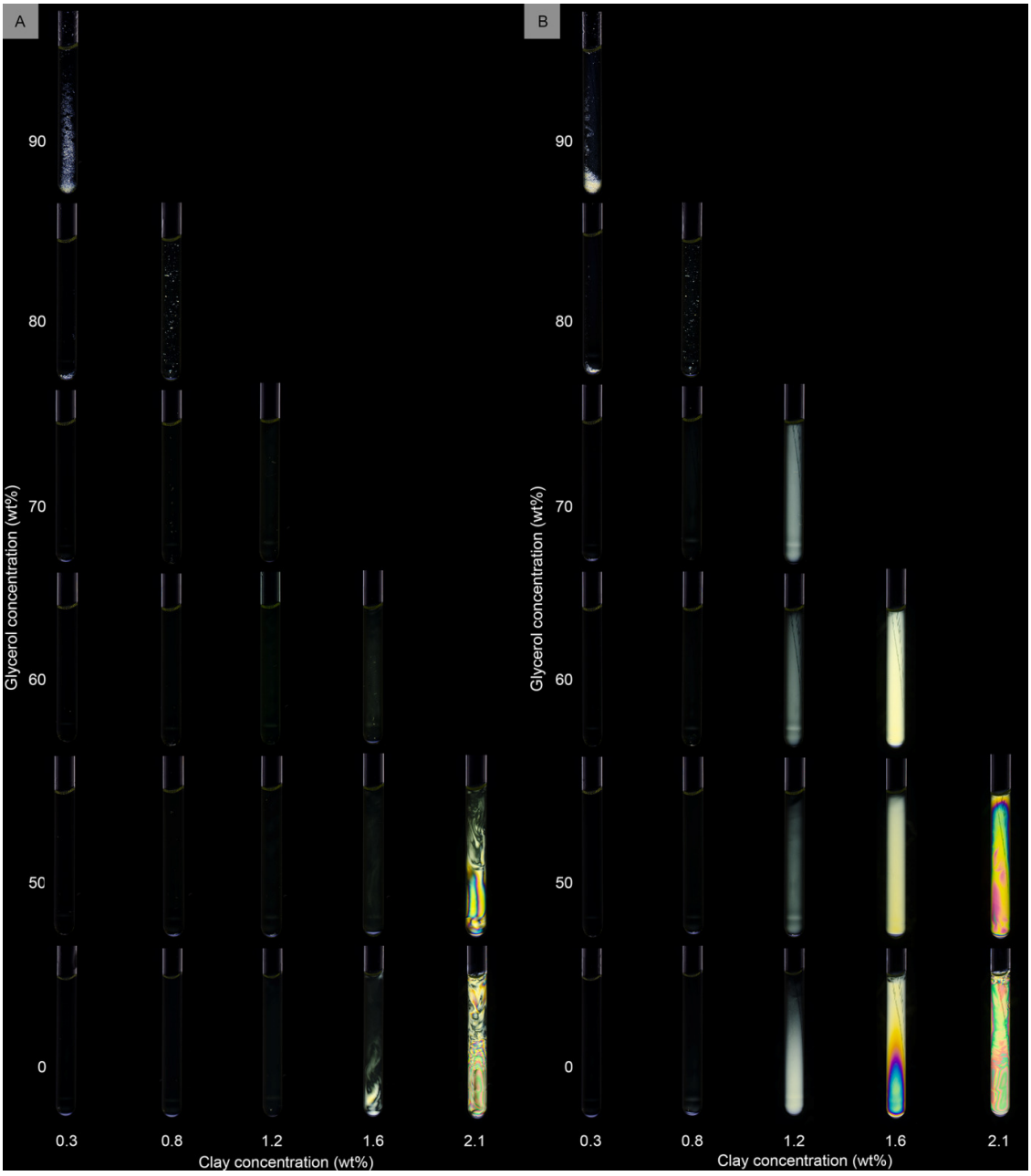

Figure 21. Nontronite clay-glycerol dispersions imaged between crossed polarizers (A) before magnetic alignment, and (B) after magnetic alignment at 14 Tesla. The salt concentration in all samples was set to 10^{-4} M NaCl.

degree of alignment is a non-linear increasing function of the magnetic field strength and volume fraction. In the case of dispersions with low clay concentrations, birefringence was only visible in the highest magnetic fields used. The maximum birefringence intensity was reached within seconds for the isotropic samples exhibiting flow induced birefringence, while the glow increased slowly enough to be quantified for samples with ≥0.5 vol% clay (top images in Figure

19). The alignment process takes much longer at higher concentrations which can be explained by the free volume around a single plate being limited by neighboring plates making the alignment a slow collective phenomena.

The effect of different clay and glycerol concentrations on the magnetically induced birefringence can be viewed in Figure 21 A-B. After magnetic alignment at 14 Tesla a striking increase in birefringence were observed in the dispersions with a clay concentration between 1.2-2.1 wt%. Before magnetic exposure, birefringent Schlieren pattering were only observed in the 1.6 wt% clay sample without glycerol, and the dispersions with 2.1 wt% clay. Schlieren patterning is one of the hall marks of nematic-like phases[60]. The dispersions with 1.2 and 1.6 wt% clay have a close to uniform birefringence without any Schlieren pattern, indicating that these dispersions form single nematic-like domain in a magnetic field. Similar observations have earlier been made in nontronite dispersions[16, 53]. The two dispersions with 2.1 wt% clay were less uniform in birefringence appearance, maintaining their Schlieren patterning. Nevertheless, the patterning experience a certain degree of change after magnetic exposure, but not enough to remove the Schlieren patterning, suggesting that the clay plates were only partly aligned in these dispersions.

The 0.3 and 0.8 wt% clay dispersions do not display any birefringence in Figure 21, but alignment has been reported to take place also in such dilute nontronite dispersions[16, 53]. Hence, it is likely that alignment takes place in the 0.3 and 0.8 wt% clay dispersions due to the strong magnetic field exposure, but the birefringence alignment relaxed before being imaged 1 min after removal from the magnetic field. Clay dispersions that are in close proximity of the nematic phase have been reported to go through a first order isotropic-nematic phase transition when exposed to magnetic fields[61, 62]. The induced nematic phase is called a paranematic phase and has been reported in dispersions of rod-shaped tobacco mosaic virus, but also for gibbsite clay sheets[61, 63]. It is therefore possible that a paranematic phase formed in the 1.2 and 1.6 wt% clay dispersions as a result of the magnetic exposure. In the future SAXS could be used to confirm that this in fact was the case.

An initial hypothesis in the project was that an increased dispersion viscosity would slow down the magnetic alignment and the birefringence relaxation of the clay plates. Magnetic alignment could not be observed in the 0.3 and 0.8 wt% clay dispersions as the birefringence in those samples relaxes within seconds, i.e. before the dispersions could be imaged. However, as mentioned above, magnetic alignment has been shown earlier in such dilute clay dispersions in much weaker magnetic fields[61, 64]. This suggest that all investigated clay-glycerol dispersions

are aligning in strong magnetic fields, but that the 2.1 wt% dispersions do so much slower as the clay dispersion gels around this clay concentration[61, 64].

An increased solvent viscosity obtained through an increased glycerol concentration does slow down the magnetic alignment kinetics and relaxation for samples with 50-70 wt% glycerol (Figure 17). However, the glycerol also affects the interparticle interactions that under some conditions decrease the clay-glycerol dispersion viscosity. Compared to the clay concentration variations, changes in glycerol concentration produce smaller changes in dispersion viscosity. Nonetheless, it is noteworthy that the glycerol concentration induced viscosity changes in Figures 15 correlated well with the observed relaxation times in Figure 17. On the other hand, there is only a weak correlation between the clay concentration induced viscosity (Figure 15) and the magnetic alignment or flow birefringence relaxation (Figure 17A). This indicates that the magnetic alignment depends on factors in the direct vicinity of each clay plate that affect the necessary rotation to enable the alignment, such as solvent viscosity and the average distance to the closest clay plates. The sample rheology, such as the moduli and viscosity, seems to be more affected by the overall microstructure, particularly whether samples have undergone phase transitions such as gelation.

The addition of 1 wt% UCST polymer to a 0.5 vol% nontronite dispersion increased the speed of magnetic clay alignment in 0.68 Tesla at room temperature and at 50°C. The increased alignment kinetics is attributed to a reduced electrostatic interaction between the plates because of polymer induced electrostatic screening.

5.6 Magnetic alignment, rheology and phase behavior in clay-salt samples

In **Paper II** the influence of clay and salt concentration on the magnetic alignment were investigated. The clay-salt dispersions in Figure 22 were imaged between crossed polarizers at different clay and ammonium bicarbonate salt concentrations, before and after magnetic exposure. Magnetically induced birefringence was observed in samples at all clay concentrations below a salt concentration of 10^{-3} M. The birefringence is very faint in the 0.3 wt% clay samples, both because the birefringence relaxes quickly and the induced birefringence becomes weaker at this low clay concentration. There are hints of weak birefringence in some of the samples with 10^{-2} M salt. In line with the findings in the clay-glycerol dispersions there was a limited correlation between the sample rheology and the possibility to magnetically align the dispersion. The samples that were defined as 'gels', by an inverted tube test, did not align. Some of the samples that were 'viscous dispersions' aligned, while others did not. Moreover, all samples defined as "dispersions" aligned except the ones with 0.3 wt% clay with 0.1 M salt.

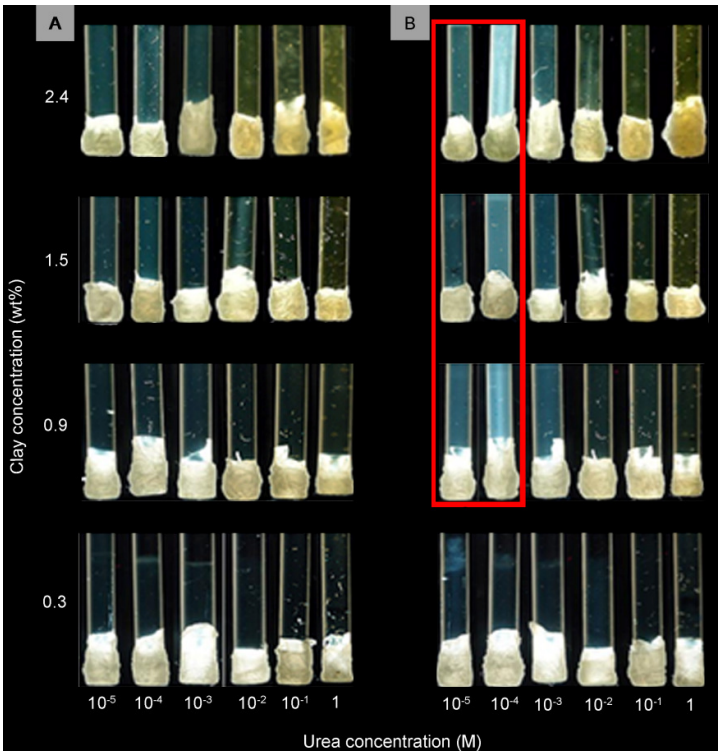

Figure 22. Pure nontronite dispersions with varied clay and urea concentration imaged between crossed polarizers (A) before and (B) after 5 minutes exposure to an 11.7 Tesla magnetic field. The urea is enzymatically converted fully to ammonium bicarbonate salt. The red frame surrounds the samples that magnetically aligned.

That a sample that is defined as a dispersion does not align while viscous samples do align clearly exemplifies that magnetic alignment is poorly correlated to the sample rheology. Instead the salt concentration, that affects screening of the surface charges and the clay-to-clay sheet repulsion, dominated the magnetic alignment behavior. Samples with a salt concentration of 10^{-3} M and below did align because they had not reached the critical level of clay-to-clay sheet aggregation that hinders alignment. Michot and co-workers[21] reported that nontronite dispersions with the same clay concentration as used in these experiments gelled around a sodium chloride concentration of 10^{-3} - 10^{-2}. Sodium chloride and ammonium bicarbonate both are salts that consist of monovalent ions, thus they are likely to similarly influence the clay dispersion phase behavior.

5.7 Liquid mass transport in clay dispersions and gels, and composites

In **Paper IV** the diffusion coefficients were measured in magnetically aligned nontronite dispersions both parallel and perpendicular to the clay plate orientation direction (Figure 23), and relatively large differences were found given the low particle concentration. As expected the diffusion coefficients were always larger in the direction parallel to the clay plate alignment. The largest difference in diffusion coefficient between these two directions was found to be 20% in the dispersion with 0.7 vol% clay. The time it takes for particles to align once placed inside the magnetic field depends strongly on the clay concentration, which puts a limit to how large directional self-diffusion anisotropy that can be practically achieved.

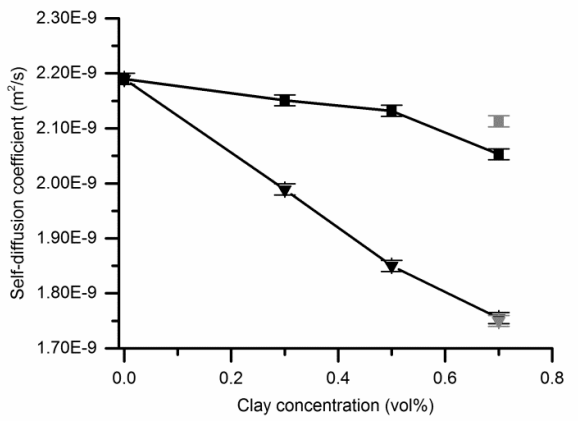

Figure 23. Self-diffusion coefficient of H_2O measured in clay dispersions with diffusion NMR in the direction parallel (squares) or perpendicular (triangles) with the magnetic field. Samples were placed for 0.5 hours in the spectrometer before measurement (black symbols), except for the 0.7 vol% clay sample where an additional time point at 36 hours is presented (grey symbols). The error bars depict the estimated experimental error.

The aim of **Paper V** was to synthesise colloidal gels with an anisotropic microstructure to control water diffusion and pressured liquid flow though the material. The orientation of the clay plates could be fixated at the point of gelation after a gradual build up of the salt concentration. This also allowed for some time for magnetic alignment of the clays before the system gelled. After the initial

clay plate gelation, additional reinforcement was provided by colloidal silica that aggregated on top of the aggregated clay network. It was not possible to measure pressurized liquid flow through magnetically oriented pure clay dispersions or gels as the pressure causes collapse of the clay-gel-plugs. Instead the clay plates were fixated in a colloidal silica matrix that made it possible to measure the speed of the liquid flow through the gels. A "tilted tube test" was used to assess the gelation. It was found that all clay-containing samples formed transparent gels 10-20 minutes after adding the enzyme. After around 1.5 hours, samples containing only silica became gradually more opaque as aggregates grew larger, resulting in gelation after around 2 h. Mixed samples with silica and clay showed a similar time dependence with regards to the appearance of sample opaqueness as the pure silica samples, independent of the clay concentration.

A maximum diffusion coefficient difference of 10% was measured in the magnetically aligned gels compared non-aligned gels, at a clay concentration of 0.5 vol% clay, and not at the highest concentration of 0.7 vol% (Figure 24). As the latter has a higher clay concentration it was expected to show a larger diffusion coefficient difference than in the 0.5 vol% gels. However both these diffusion measurements and the birefringence observations indicate that gels with 0.7 vol% clay have a higher degree of clay aggregation. This observation is attributed to the high clay concentration in combination with the presence of salt. In combination these two factors might have induced clay plate face-to-face aggregation.

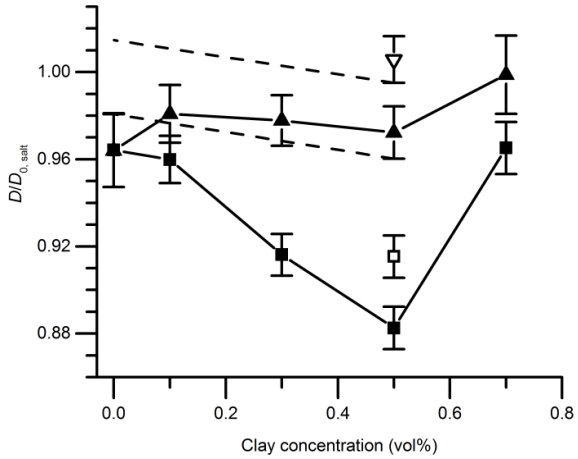

Figure 24. Relative self-diffusion of water measured with NMR spectroscopy in gels with magnetically aligned clay plates (triangles) or non-aligned gels (squares). Gels are symbolized as follows: Pure colloidal silica (4.1 vol%) and collodial silica mixed with clay (filled symbols) and pure clay (open symbols). $D_{0,salt}$ is the self-diffusion in pure salt solution. The black dashed lines designate the limits of the decline in diffusion coefficient in the magnetic gels allowed for by the experimental error. Error bars depict the propagated standard deviation of the calculated diffusion coefficient described in **Paper V**.

In Figure 25, the liquid permeability is higher in the magnetically aligned gels compared to non-aligned gels, with the exception of the pure silica gels. The effect is attributed to the effect of clay alignment as discussed in the diffusion section above. Interestingly, the permeability increased in the aligned gels of low clay content compared to pure silica gels, even though the particle concentration is increased. Also, there is a permeability maximum at 0.3 vol% clay although the relative difference in permeability between aligned and non-aligned gels increases with clay concentration, reaching a factor of two at 0.7 vol%. It is possible that the increased permeability at low clay concentration observed in the aligned gels relative the pure silica gels is caused by two mechanisms. Firstly channels of lower mass transport resistance are formed when clays are added to gels, and secondly these channels are aligned in magnetic fields. The clay plates deplete the surrounding region of silica particles by adsorption. In the non-aligned gels a similar but weaker effect is observed in the absence of clay alignment as the permeability remains unchanged even though the clay particle content is increased up to 0.3 vol%.

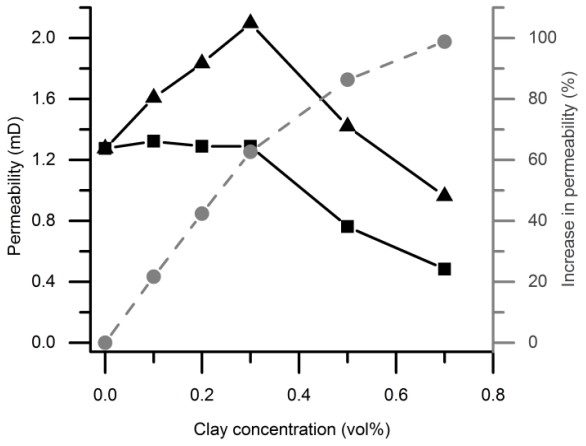

Figure 25. Fluid permeability of gel plug in column with salt solution on top (black curves), comparing permeability of gels with magnetically aligned clay plates (triangles) and non-aligned gels (squares). The grey curve show the relative percent increase in permeability for aligned relative the non-aligned gels. Gels are made of either pure colloid silica or silica mixed with varying amounts of clay.

Above this concentration we propose that the increased clay concentration decreases the permeability due to the following. Adding more than 0.3 vol% clay does not result in further channel formation through the silica network as all silica already is associated with the clays. Instead an increasing clay concentration reduced the permeability by provide surfaces that bind water and thereby makes the effective volume available for flow smaller.

5.8 Aggregation, microstructure and liquid mass transport in silica-polyNIPAM gels

In **Paper VI** a sol-gel method was demonstrated for bulk scale synthesis of a nanocomposite with temperature switchable liquid permeability properties. The nanocomposite demonstrated that nanoparticles can be used to make aggregated microstructures with dynamic liquid mass transport characteristics. This material can be used in applications ranging from liquid flow valves in nanotechnology, to bulk scale synthesis of materials for use in membrane technology. The material was made by mixing dispersions of poly(N-isopropylacrylamide) (PNIPAM) microgels and colloidal silica sol. Next the mixed dispersion was destabilized by adding a NaCl solution, which resulted in gelation and fixation of the microgels in an aggregated colloidal silica matrix. Various aspects need to be considered when synthesizing functional porous materials for liquid flow control. Liquids flowing through nano- and microporous materials expose the structures to hydrodynamic stress that in some cases can cause compression and collapse of the material. Moreover, the gels are exposed to considerable mechanical stress when the microgels contract and expand, as the temperature is varied above and below the LCST. Figure 26A-D shows the composite silica PNIPAM gels with different microgel concentrations ranging between 0 and 2.1 wt%. All gels had a colloidal silica concentration of 22 wt% and salt

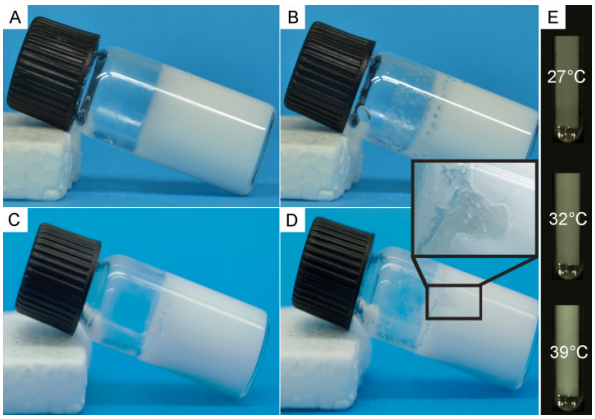

Figure 26. Composite silica gels and a PNIPAM dispersion at different temperatures. The PNIPAM concentration and temperature in the composite gels are as follows (A) 0 wt%, 40°C (B) 1.4 wt%, 40°C (C) 2.1 wt%, 25°C (D) 2.1 wt%, 40°C. The inset shows a crack that formed in the gel with 2.1 wt% PNIPAM when the temperature was increased. (E) A 0.7 wt% PNIPAM microgel dispersion viewed in a glass capillary at different temperatures. The dispersion opaqueness increased noticeably around and above 32 °C.

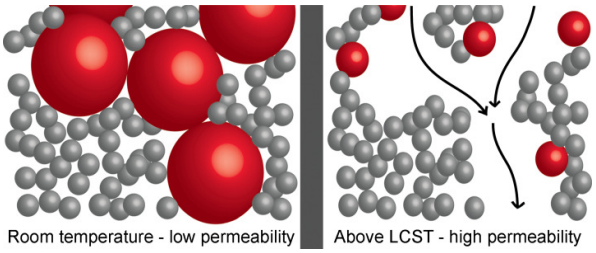

Figure 27. Schematic drawing of the microstructure and liquid flow in composite gels consisting of colloidal silica (grey particles) and PNIPAM microgels (red particles), at room temperature and above 32°C, which is the LCST of PNIPAM. The black arrows illustrate liquid flow through the pores following microgel (PNIPAM) shrinkage.

concentration of 0.5 M NaCl, under which conditions gelation occurred in 1-1.5 hours. The mechanical stability of the gels was improved by being at rest for one week before performing inverted tube tests or permeability experiments. The improvement is attributed to Oswald ripening, which redeposited dissolved silica at the contact points between the particles. Figure 27 illustrates the envisioned final material structure as the microgels are locked into place within a colloidal silica matrix.

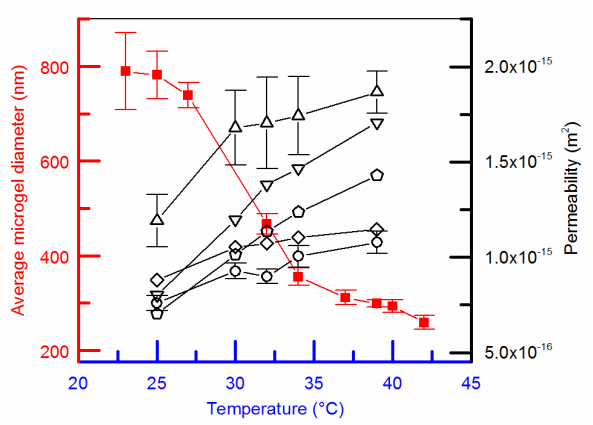

Figure 28. The temperature dependence of the PNIPAM microgel size (red curve) and water permeability of the silica-PNIPAM gels (black curves) with the following PNIPAM concentrations: 0 wt% (circles), 1.0 wt% (diamonds), 1.4 wt% (triangles pointing up), 1.6 wt% (triangles pointing down), and 1.8 wt% (pentagons). The error bars depict standard deviations. For clarity, the water permeability error bars are omitted for all gels except the ones with PNIPAM concentrations of 0 and 1.4 wt%.

At 25°C, all gels shown in Figure 26 had a macroscopic homogenous opaque white appearance. The appearance and mechanical integrity of the gels remained at 40°C for all gels except for the gel with 2.1 wt% PNIPAM (Figure 26C-D). This gel developed millimeter-sized cracks in the interface between the glass wall of the vial and the gel (see Figure 26D-inset). The same temperature change in a composite gel with 3.27 wt% PNIPAM resulted in shrinkage and collapse of the entire gel (data not shown). Hence a

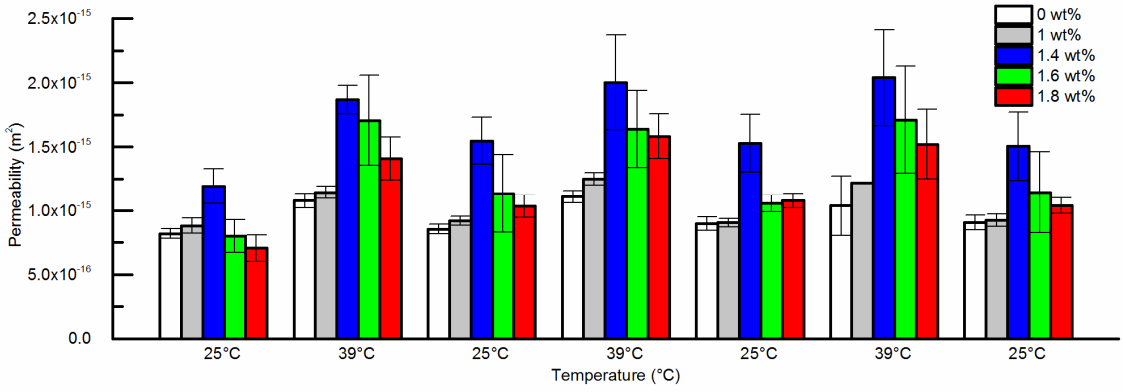

Figure 29. Water permeability in composite silica–PNIPAM gels at different temperature and PNIPAM concentrations. A reversible change in permeability was observed over several consecutive cycles of temperature change. The error bars depict the standard deviations.

PNIPAM concentration of around 1.8 wt% was the upper limit that allowed the composite gels to withstand the temperature-induced microgel contractions. Uncertainty remains about the distribution of the microgels within the composite gels. The microgels would not be visible in transmission electron microscopy (TEM). Even so, in future experiments, we hope to view the distribution of the microgels indirectly by TEM imaging of the silica particle network around the microgels in embedded sections from the composite gels.

Aqueous non-gelled dispersions of PNIPAM microgels without silica had a characteristic "cloud point" at the expected LCST (Figure 26E). This characteristic was observed as a more opaque sample at 32 compared 27°C due to increased scattering of visible light. The dispersion opaqueness increased further at 39°C. The scattering resulted from a change in the hydrophilic-hydrophobic nature of the PNIPAM in the microgels: At around 32°C, the hydrophobicity increased to the point where the microgels expelled much of their water content[30]. The DLS results shown in Figure 28 corroborate the visual observations, as the temperature region of greatest size change is centered on 32°C. The average gel diameters at 25 and 39 °C were 782 and 299 nm, respectively, corresponding to a 94.4% reduction in the average microgel sphere volume, similar to previously reported results[65]. Hypothetically, this opens up a 483 nm pore space for liquid flow between the silica matrix and the contracted microgel.

As Figure 28 illustrates, changes in temperature and microgel size affect the water permeability of the composite gels. When the microgels contracted, the permeability increased, and the effect was already significant between 25 and 30°C, i.e. several degrees below the LCST of 32°C. The permeability increased with increasing temperature also in the pure silica gels, suggesting that part of the increase was due to viscosity changes in the permeating liquid.

The composite gels can be used as liquid flow valves to reversibly adjust the flow of water coming through the gels (Figure 29). In the pure silica gels, the permeability increased by 42% the first time the temperature was increased from 25 to 39°C. The corresponding changes in the composite gels with 1, 1.4, 1.6 and 1.8 wt% PNIPAM were permeability increases of 30%, 57%, 113% and 61%, respectively. The second and third time the temperature was increased from 25 to 39 °C, the average permeability increased 22, 35, 32, 53 and 69% for the gels with 0, 1, 1.4, 1.6 and 1.8 wt% PNIPAM, respectively. The largest relative changes in permeabilities occurred during the first temperature cycle, suggesting that irreversible changes occurred during that cycle. The culprits could range from loss of microgels at the surfaces of the gel or misalignment of the microgels within the pores as they shrink and reswell, leaving small pores

next to the microgels even in their swelled state. Formation of microcracks can also be an explanation; however, no cracks could be seen in the samples, and the gels remained mechanically strong during the entirety of the permeability measurements. The gels with 1.4 and 1.6 wt% PNIPAM displayed the largest absolute and relative change in permeability, respectively. This result suggests that the percolation threshold for a connected pore space has been reached around this microgel concentration, allowing for a continuous flow through the whole sample volume.

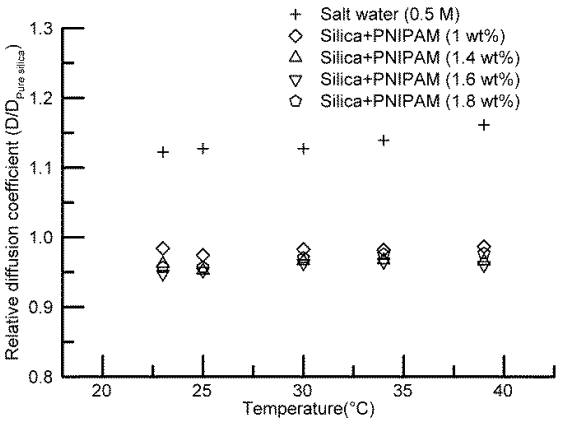

Figure 30. Relative diffusion coefficients at different temperatures in composite gels with 22 wt% silica and varied PNIPAM concentrations. The relative diffusion coefficients were obtained by normalizing to the diffusion coefficient in the pure silica gels.

As expected the diffusion coefficient was higher in the pure salt water than in the gels due to the obstructing effect of the gel microstructure and the water-silica or -PNIPAM surface interactions (Figure 30). A normalization for temperature shows that the relative water diffusion show no significant decrease at increased PNIPAM concentrations. As the relative diffusion remained constant over the whole temperature range the contraction of the microgels did not in itself appear to affect the water diffusion. This result suggests that the diffusion rate depends on temperature and the concentration of solid material, not on the material's microstructure. The results are nicely explained by studies of permeability in polymer films containing dispersed microgels by Zhang and Wu, where the permeability of small molecules through films containing swollen and contracted microgels was the same, but differed significantly for molecules significantly larger than water[66].

The normalized water diffusion decreased in all gels, as expected due to the obstruction effect. Furthermore, the surface charge of the silica particles and the microgel polymer network bind water which effectively slows down water diffusion. We and others have previously investigated both these effects[16, 67, 68].

5.9 Aggregation, microstructure and liquid mass transport in silica gels

In **Paper VII** and **VIII** experiments and simulations were used to investigate how the particle volume fraction and aggregation behavior affect the microstructure of dilute nanoparticle gels. Moreover it was investigated how these factors affected the water diffusion and liquid permeability.

In **Paper VII** the simulated network structures and mass transport results were compared with experimental results from nanoparticle silica gels consisting of amorphous SiO_2 spherical primary particles with an average diameter of 22 nm. The gels were made by a sol-gel process in which NaCl solution were added to optically transparent nanoparticle dispersions. This caused particle aggregation and the formation of opaque white gels with covalent siloxane bonds between the particles. Silica nanoparticles were chosen because they have strong contrast in TEM and they form mechanically robust gels that do not collapse during permeability measurements.

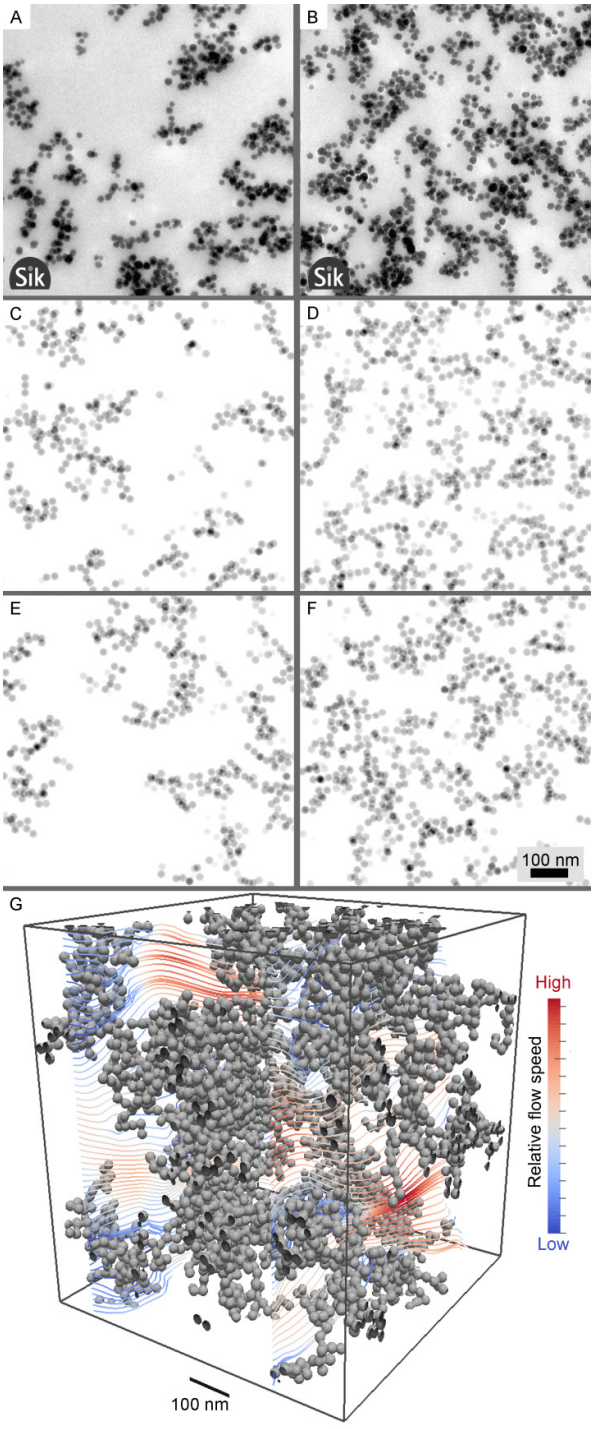

Figure 31. Experimental (A & B) and *in-silico* (C-F) TEM micrographs of 60 nm thick particle gel sections with a particle volume fraction of (A, C & E) 0.023 and (B, D & F) 0.041. The *in-silico* TEM images in C & D and in E & F & G had, respectively, a 1 and 10^{-4} probability of aggregation. Figure 2G shows an *in-silico* generated particle 3D structure with flow line visualization of relative flow speeds throughout the structure. Such simulations were used to calculate the permeability and diffusion through the simulated structures.

To investigate how aggregation conditions affect the pore size and mass transport *in-silico* generated structures were made with diffusion (DLCA) and reaction limited cluster aggregation (RLCA) algorithms. These algorithms simplify the physics of aggregation by reducing the process to diffusing particles and an aggregation probability (P) at each inter-particle collision. DLCA collisions results in an aggregation event at every collision (P=1) while for RLCA only a small fraction of the collisions leads to aggregation (P<<1)[69, 70]. DLCA controlled processes are reported to yield more open and thin stranded structures compared to RLCA. Figure 31 compares the particle network structures of experimental TEM and *in-silico* TEM images, where the *in-silico* images were reconstructed from light projections of sections of the *in-silico* structures. The structure of colloidal silica gels has been investigated in numerous studies by methods such as TEM[16], small angle X-ray scattering[32] and light scattering[71]. Most studies indicate that the silica particles aggregate through processes that can be described by RLCA-process[32]. There are no previously reported investigations on the pore size distributions in structures with varying particle concentration between the aggregation limits of DLCA and RLCA.

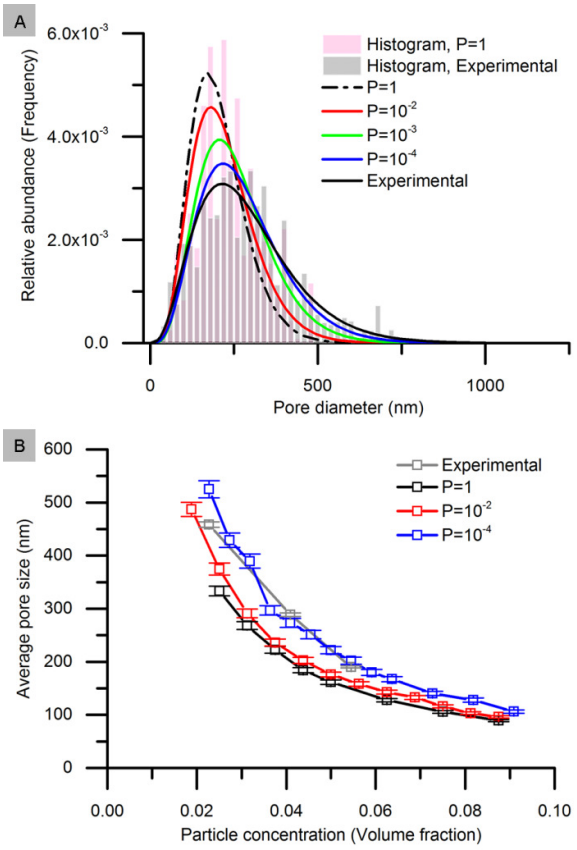

Figure 32. Pore size analysis in colloidal silica gels made in simulated and real TEM images. (A) Fitted pore size distributions in gels with a silica volume fraction of 0.041 as a function of aggregation probability (770 nm box size), together with the pore size histograms obtained from real TEM images and images made from simulated structures (P=1). (B) Average pore size as function of silica concentration for varying aggregation probabilities (770 nm box size). The error bars represent the 95% confidence interval of the estimation.

In Figure 32 the pore size distributions obtained from the *in-silico* gel structures is compared with the experimental silica gels at a fixed particle concentration. Indeed, the experimentally measured pore size distribution bears most similarity with simulated structures with $P=10^{-4}$, which is in the strong RLCA regime. Several studies have found that silica particles aggregate through a RLCA-like process and that only minute structural changes can be expected at lower aggregation probabilities[48].

A change in the aggregation probability from 1 to 10^{-4} resulted in a 30 % increase in the average pore size (150 to 200 nm), as P is decreased from 1 to 10^{-4} (Figures 32A).

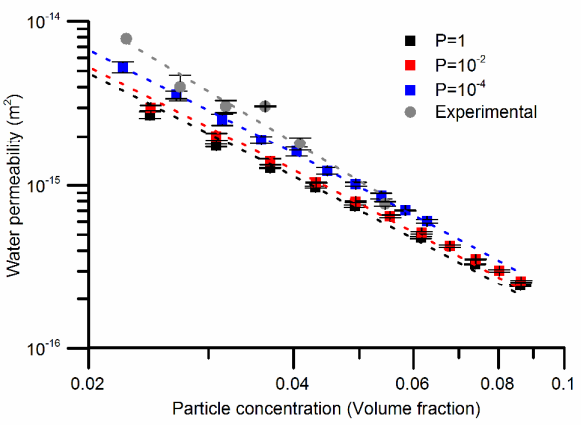

Figure 33. Experimentally measured (grey filled circles) and LB-simulated water permeability of gels as a function of particle concentration. Permeability simulations were made in aggregated particle structures generated through simulations with different aggregation probabilities (P). The permeability in the simulated structures could all be fitted (dotted lines) by a power-law relationship. The error bars represent the standard deviation.

Figure 33 shows that the experimentally measured permeability is fairly well described by permeability Lattice Boltzmann (LB)-simulations in *in-silico* generated structures with an aggregation probability of 10^{-4}. The permeability as a function of silica concentration for all simulated aggregation probabilities is well described by the Kozeny-Carman equation (Equation 16), The Kozeny-Carman equation is commonly to used for liquid permeability prediction[72],

$$k = \frac{\phi_{pore}^3}{36K_{kc}(1-\phi_{Pore})^2} d^2 \qquad \text{[Equation 16]}$$

where K_{kc} is the empirically derived Kozeny-Carman constant, d is the particle diameter, and porosity (ϕ_{pore}) that is the volume faction of the sample that is taken up by pores. The experimentally measured power law exponent is -2.5 which is significantly different ($p<1\times10^{-3}$) from the simulated results all having a power law exponent of -2, consistent with the Kozeny-

Carman equation at high porosity. This suggests that additional factors not included in the DLCA and RLCA models could be of importance to predict permeability in colloidal silica gels. One such factor could be structure rearrangements after particle-particle bonding events. This factor could give changes in the microstructure that varied with the particle concentration, which would explain the permeability behavior. Structure rearrangements after aggregation are more likely to occur at low particle concentration as the aggregates under these conditions form less dense and weaker structures which are more prone to aggregate detachment and angular rotation of the aggregates while still bond. Rearrangements will cause consolidation of the networks strands, larger pores and larger permeabilities and these processes are not considered in the DLCA-RLCA algorithms. Another possible explanation is structural changes due to the pressure exerted by the flowing fluid inside the gel. From this effect, one would expect an increased permeability since large pores would be widened by the force from the fluid. The effect is also expected to be larger at lower particle concentrations when the gel is less stiff, which agrees completely with the experimental data. To investigate this effect computationally, a more elaborate model than the present would be necessary, allowing for deformation of the structure.

Paper VIII showed that large differences in microstructure characteristics and liquid permeability can be achieved by varying the primary particle size of aggregating colloidal silica. Three different sizes of primary particles were investigated (22 nm, 5 and 3.6 nm) and all silica gels had the same silica concentration (volume fraction: 0.041). The transparent silica dispersions were gelled by adding NaCl. A visual inspection of the samples after gelation showed that the opacity of the gels increased with particle size, with the smallest particle size yielding transparent gels, while the largest size formed white densely opaque gels. This observation indicated that the microstructure formed by the larger particles had a larger characteristic length scale that interacted and scattered light more efficiently. Indeed, the TEM

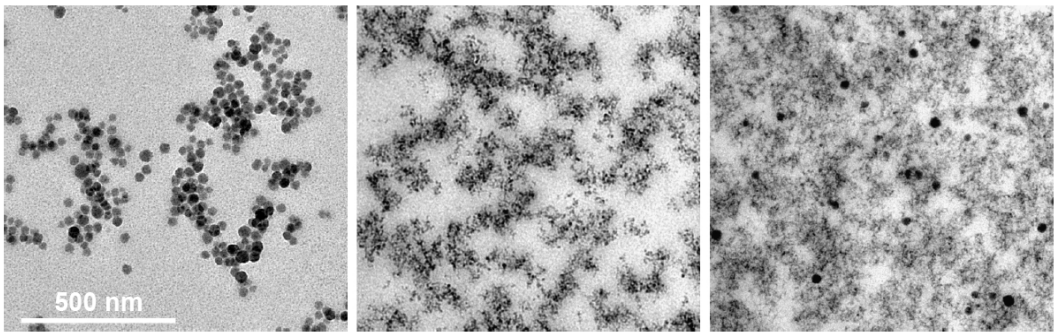

Figure 34. TEM micrographs of embedded and sectioned (70 nm) colloidal silica gels. The average silica particle diameter before aggregation are, from left to right, 22 nm, 5 and 3.6 nm.

micrographs in Figure 34 shows that the pore size varies considerably as a function of the primary particle size. One measure of the pore size used in **Paper VIII** is the volume-weighted mean volume (VWMV)[73]. This measure has the benefit of being independent on the pore shape. The pore size measurements (Table 1) shows that the pore size in the gels with the largest particle size was more than a magnitude larger compared to the gels with the smallest particles. The liquid permeability is often greatly affected by the pore size at these length scales. The different gel types had very small differences in their water diffusion coefficients. This could be explained by that the diffusion of the small water molecules in the relatively large pores of the silica gels is mainly dependant of the volume fraction of the silica particles that was the same for all gels. The flow speed in the gels with the largest particle size was 400-500% faster than in the gels with the other particles sizes. Furthermore, the flow speeds in the gels with a primary particle size of 5 and 3.6 were not significantly different even though their pore sizes differed 4-5 times in size. The lack of difference is also illustrated by the dimensionless Péclet number (Pe) of the different gels. The Péclet number is defined as the ratio between the flow and the diffusion contribution to the total mass transport, and it can be calculated by the following equation,

$$\mathrm{Pe} = \frac{\nu \mathrm{L}}{\mathrm{D}} \qquad \text{[Equation 17]}$$

In Equation 17, ν denotes the flow speed in m/s, and D is the diffusion coefficient. The gel plug thickness (L) was 3.0 cm. The Pe in the gels with the largest particles was around 0.74 which means the liquid mass transport in the gels can be expected to be slightly dominated by diffusion-like transport, however, the Pe of the two other gels (Pe = 0.1) was the seven times smaller than for the gels with large particles (Table 1). It appears like the mass transport in the gels with the two smaller particle sizes were dominated to a higher extent by diffusion-like mass transport. As diffusion is mainly controlled by the volume fraction of particles in colloidal particle systems with an isotropic microstructure, this could explain why the transport of liquid through the gels with the two smaller particle sizes displayed no differences.

Primary particle size (nm)	**VWMV Pore size** (nm)	**Water diffusion coefficient** ($\times 10^9$ m^2/s)	**Flow speed (mm/day)**	**Péclet number (Pe)**
2	530 ± 120	2.04 ± 0.0204	2.5 ± 0.091	0.74
5	120 ± 20	1.99 ± 0.0199	0.59 ± 0.043	0.10
3.6	39 ± 6.3	1.98 ± 0.0198	0.58 ± 0.039	0.10

Table 1. Measured pore size and liquid mass transport coefficients in colloidal silica gels (**Paper VIII**). The error values indicate the standard deviation.

CHAPTER 6

Potential applications of synthesized materials

This chapter treats two potential applications of the synthesized materials, as opposed to the other chapters that mainly have discussed the model system uses of the materials.

6.1 Colloidal silica-clay composites for ground stabilization and barrier formation

Mechanically unstable soils can be found at many areas around the world, such as muddy hillsides, river banks, and soils in connection to mining, tunnels and other construction operations. Without the right precautions such grounds can be treacherous as they may collapse with little warning, risking human lives and infrastructure. In some cases it is beneficial to stabilize the soil by injecting stabilization agents into the ground. Other times the soil is contaminated by chemical waste, in which case it is good to decrease the flow of water through the soil to avoid spreading the contamination. Colloidal silica gels that are treated in **Paper V** and **VII-VIII** are today used for ground stabilization and to reduce the soils liquid permeability[74]. Typically the silica sol is mixed with a salt solution followed by ground injection before the mixture gels. However, if the ground water flow is high through the cracks and pores of the injection site, the silica gel may be rinsed away, or diluted to a mechanically week state before gelation. **Paper V** offer a tentative solution to this problem as the *in-situ* gelation of colloidal silica-clay dispersions gels goes through a two-step gelation mechanism. The gradual increase of the salt concentration quickly causes a clay induced increase in the mixture's viscosity that makes it less likely to be rinsed away by the intense underground water flow. Finally the mixture gels (seconds-minutes) forming a relatively weak gel. As the salt concentration increases further, the silica particles aggregate (minutes-hours) onto the clay particle network, effectively reinforcing the aggregated clay structure. The formed silica-clay composite forms a relatively strong gel that can stabilize, or decrease the permeability of the soil. The gelation speed of the two different steps can be tuned by adjusting the enzyme concentration, urea concentration, particle type and particle concentration of the mixture.

6.2 A self-assembling colloidal silica - microgel liquid flow valve

Small liquid flow valves are used to control liquid flow in high-performance liquid chromatography[75], microfluidics[76] and in controlled release[65]. Often these valves consist of parts that are tedious to assemble, which is why self-assembling vales would be ideal. Such a valve-material was constructed by a sol-gel process in **Paper VI**. The material was made from temperature responsive microgels dispersed in a colloidal silica matrix. These microgels contracted and swelled reversibly in response to temperature changes, which opened up and closed pores for liquid flow through the material (See Figure 27). One benefit with the composite is that it can be gelled into any shape, for example to form a plug in a tube. Previously reported materials with similar functions have been limited to films[65], while the material in **Paper VI** can be made into any geometrical shape. The sol-gel process can, with relative ease, be adapted to a great range of inorganic particles that are available on the market[77]. In addition, the literature offers a great range of microgels that are responsive to many types of triggers, such as different temperatures[65], pH[78], glucose concentration[79], and so on. Thus it can be envisioned that composite gels with triggered liquid permeability can be made for a range of triggers and applications.

CHAPTER 7

Conclusions

Has this thesis answered the question "How can a material synthesis method be designed to reproducibly produces materials with the correct pore-structure and the intended function?" Given the scope of this question it is no surprise that the thesis has not been able to fully answer this question. Yet, the studies performed in the thesis have in part answered the question in relation to liquid mass transport in dilute nanocomposite materials, and colloidal gels overall.

This work confirmed that clay plates adsorb water on their surfaces equivalent to several times its own particle volume, and that small concentrations of exfoliated clay particles cause large reductions in the diffusion coefficient of water. For example, the plate shaped nontronite particles used in **Paper V** reduced the water diffusion coefficient sixty times more per volume fraction particles compared to the spherical silica particles. However, in the presence of large salt concentrations dilute clay gels with particle concentrations close to the sol-gel transition are prone to clay plate face-to-face aggregation. In this aggregation state the clay plats bind less water and provide less hindrance to the water diffusion.

In **Paper I-V** it was demonstrated that nontronite plates can be magnetically aligned. An interesting observation was that the magnetic alignment of the clay dispersion and the dispersion rheological behavior were poorly correlated. The magnetic alignment was controlled by factors acting in direct vicinity of each dispersed clay plate that govern the necessary rotation during the alignment. These factors include solvent viscosity, clay plate crowding related to the clay concentration, and electrostatic interactions that were varied mainly by changing the salt and glycerol concentration. Conversely the sample rheology, such as the moduli and viscosity, depends more on phase transitions or aggregation events that act on the whole sample. Plate alignment had a large influence on the optical birefringence behavior of the material, but most importantly in the context of this study, it had significant influence of the liquid mass transport through the material. For example, in a magnetically aligned 0.7 vol% nontronite dispersion the water diffusion coefficient was 20% larger in the direction parallel to the clay alignment compared to the perpendicular direction. A model was developed to predict the diffusion coefficient in magnetically aligned dispersions and gels. The model took into account clay plate size, concentration, degree of plate alignment and water bounding to the clay surfaces.

In **Paper V** it was shown that magnetic alignment can be used to vary the pressure induced liquid permeability in nanocomposite gels made from silica and nontronite. Gels with 0.7 vol% clay that were aligned had a doubled permeability compared to the non-aligned gels. Comparing gels with a clay concentration between 0-0.7 vol%, the magnetically oriented gels had a maximum water permeability and self-diffusion coefficient at 0.3 and 0.7 vol% clay, respectively. Hence the specific clay concentration resulting in the highest liquid flux was pressure dependant. In summary both the aggregation state and magnetic alignment can used to control both liquid diffusion and permeability in clay containing materials.

In **Paper VII** and **VIII** experiments and simulations were used to investigate how the size and concentration of spherical nanoparticles, and aggregation behavior, affect the microstructure and liquid mass transport in dilute colloidal silica gels. The experimentally characterized microstructure and liquid mass transport properties of the silica gels were found to be most similar to simulated structures generated by algorithms in the strong RLCA regime. The results were used to derive microstructure and mass transport correlations for a wide set of particle aggregation conditions. These correlations are of general application when predicting the pore size, liquid diffusion and permeability in nanoparticle materials. The correlation for the average pore size is valid for any particle size as long as the aggregation of the investigated system can be described by DLCA-RLCA algorithms. An important observation was that the difference in average pore size at all particle concentrations was only 30% between the limits of DLCA and RCLA. **Paper VIII** showed that much larger differences in pore size can be obtained at a fixed particle volume fraction by varying the particle size. For example, by increasing the primary particle size from 3.6 to 22 nm the pore size increased 1,350 %.

In **Paper VI** a nanocomposite gel material was synthesized. The composite consisted of poly(N-isopropylacrylamide) microgel dispersed in a colloidal silica matrix. By heating the composite above 32°C the microgels contract which allows for liquids to flow in the open pore space between the matrix and the microgels. Composites with a microgel concentration between 0 and 1.8 wt% could withstand repeated temperature variations. The permeability more than doubled (+113%) in the gels with 1.6 wt% microgels when increasing the temperature from 25-39°C. The gel composite could be used as a temperature-responsive liquid flow switch in membranes, drug delivery or advanced nanotechnology devices.

In summary, this thesis treats the aggregation-microstructure-liquid mass transport relationship in nanocomposite materials. Several factors that could affect this relationship were explored to

establish a number of model materials, characterization techniques, and microstructure and liquid mass transport models. The observations, synthesis methods and models produced in this thesis merits consideration when designing microporous materials, especially in applications were the liquid mass transport through the pores are important.

Acknowledgements

The VINN Excellence Centre SuMo Biomaterials with financial support from VINNOVA is acknowledged for Financial Support.

I meet many fantastic people during my years as a PhD student and I would to acknowledge and with gratitude thank:

Everyone at Applied Chemistry for creating a great atmosphere to work in. Thank you for providing advice and lively discussions in the lunch room, at work shops and conferences.

My supervisor Magnus Nydén for taking me in as a PhD student. You have given me advice and inspiring new perspectives. You also gave me more freedom to explore than most supervisors would have dared to give, in short thank you for believing in me.

My co-supervisor Johan Bergenholtz for all your advice, expertise and interesting discussions.

My examiner Krister Holmberg for inspiration, expertise and help with many practicalities, and for looking out for me in general.

Romain Bordes my roommate, for good laughs, help with things in the lab and discussions about an endless number of scientific questions and other things.

Lars Nordstierna, Anette Larsson, Per Rudqvist, Anders Palmqvist, Anders Mårtensson, Sven Engström, Jonatan Bergek, Sven Engström and Gavin Jeffries for your help, advice, expertise and interesting discussions.

My Master thesis students Mojtaba Siahpoosh, Shiyu Geng, Hanzhu Zhang, Yuman Li, Cecilia Doung and Cecilia Lu. It was a privilege to supervise your projects and I would like to thank you for everything you taught me as a person, researcher and supervisor. Without your hard work this thesis would have been less interesting, and certainly thinner.

Ann Jakobsson for help with numerous administrative matters and many interesting discussions.

Kurt Löfgren for your skilled help with building equipment for experiments and interesting discussions.

All SuMo center university and industry partners. I would especially like to mention Michael Persson, Johan Lif and Magnus Palmlöf at AkzoNobel; Mariagrazia Marucci, Susanna Abrahmsen-Alami, Johan Hjärtstam and Johan Arnehed at AstraZenca; Jenny Fäldt at SCA; Annika Altskär, Mats Stading and Diana Gomez Martinez at SP Food and Bioscience for all practical help, advice, discussions and for making me feel very much welcome when I visited you.

My co-authors for productive collaborations: Melanie Ramiasa, Katherine Locock, Magnus Röding, Charlotte Hamngren Blomqvist, Tobias Gebäck, Matias Nordin, Ann-Marie Hermansson, Stefan Gustafsson, Niklas Lorén, Eva Olsson, Sergey Dvinskikh, Alexander Idström, Markus Andersson Trojer, Azmi Mohamed, Julian Eastoe, Ye Li, Henrike Häbel, Aila Särkkä, Mats Rudemo, Diana Bernin, Hillary Fabich and Jurgita Kazlauske.

Ellis Meng at University of Southern California in Los Angeles for letting me visit her lab during several months as a visiting research scholar. I would also like to thank all the other lab members of Ellis's lab for advice, a welcoming atmosphere and practical help. I would like to especially mention Tuan Hoang, Brian Kim, Kee Scholten, Alex Baldwin, Roya Sheybani, Curtis Lee, Angelica Cobo, Jessica Ortigoza, Seth Hara, Lawrence Yu and Ahuva Weltman. Thank you Chalmersska Forskningsfonden and Stiftelsen Lars Hiertas Minne for providing funding for this research visit.

Lars Rokkjaer for much help and insight, and for helping me discover new tools to view myself and others.

Fredrik Gunnarsson, Alireza Movahedi and Adele Khavari, I really value your friendship and our discussions.

Finally I would like to thank my family, especially my wife Suzanne Nguyen and son Thor for your love, and the dreams and inspiration you provide me with.

References

1. S. Chu and A. Majumdar, Nature, 2012, 488, 294-303.
2. H. Buhaug and H. Urdal, Global Environmental Change, 2013, 23, 1-10.
3. K. Modig, S. Drefahl, T. Andersson and A. Ahlbom, European Journal of Epidemiology, 2012, 27, 139-145.
4. L. T. Raynolds, D. Murray and J. Wilkinson, Fair trade: The challenges of transforming globalization, Routledge, 2007.
5. T. Gleeson, W. M. Alley, D. M. Allen, M. A. Sophocleous, Y. Zhou, M. Taniguchi and J. VanderSteen, Groundwater, 2012, 50, 19-26.
6. D. P. Van Vuuren, B. J. Strengers and H. J. De Vries, Resources Policy, 1999, 25, 239-255.
7. B. D. Ratner, Biomaterials science: An introduction to materials in medicine, Academic press, 2004.
8. R. Malik, D. Burch, M. Bazant and G. Ceder, Nano Letters, 2010, 10, 4123-4127.
9. G.-G. Park, T.-H. Yang, Y.-G. Yoon, W.-Y. Lee and C.-S. Kim, International Journal of Hydrogen Energy, 2003, 28, 645-650.
10. K. Kabiri, H. Omidian and M. Zohuriaan-Mehr, Polymer International, 2003, 52, 1158-1164.
11. B. P. Timko, M. Arruebo, S. A. Shankarappa, J. B. McAlvin, O. S. Okonkwo, B. Mizrahi, C. F. Stefanescu, L. Gomez, J. Zhu and A. Zhu, Proceedings of the National Academy of Sciences, 2014, 111, 1349-1354.
12. M. Larsson, J. Hjärtstam, J. Berndtsson, M. Stading and A. Larsson, European Journal of Pharmaceutics and Biopharmaceutics, 2010, 76, 428-432.
13. T. J. Barton, L. M. Bull, W. G. Klemperer, D. A. Loy, B. McEnaney, M. Misono, P. A. Monson, G. Pez, G. W. Scherer and J. C. Vartuli, Chemistry of Materials, 1999, 11, 2633-2656.
14. G. Maitland, Current Opinion in Colloid & Interface Science, 2000, 5, 301-311.
15. H. Okabe and M. J. Blunt, Physical Review E, 2004, 70, 066135.
16. C. Abrahamsson, L. Nordstierna, J. Bergenholtz, A. Altskär and M. Nydén, Soft Matter, 2014, 10, 4403-4412.
17. G. Bell, Transactions of the Faraday Society, 1964, 60, 1752-1759.
18. F. Madsen, Clay Minerals, 1998, 33, 109-129.
19. C. Yang, W. Smyrl and E. Cussler, Journal of Membrane Science, 2004, 231, 1-12.
20. S. S. Ray and M. Okamoto, Progress in Polymer Science, 2003, 28, 1539-1641.
21. L. J. Michot, I. Bihannic, S. Maddi, S. S. Funari, C. Baravian, P. Levitz and P. Davidson, Proceedings of the National Academy of Sciences, 2006, 103, 16101-16104.

22. E. Tombacz and M. Szekeres, Applied Clay Science, 2004, 27, 75-94.
23. P. Porion, A. M. Faugere, L. J. Michot, E. Paineau and A. Delville, Langmuir, 2010, 26, 7035-7044.
24. O. Ballet and J. Coey, Physics and Chemistry of Minerals, 1982, 8, 218-229.
25. L. Onsager, Annals of the New York Academy of Sciences, 1949, 51, 627-659.
26. R. K. Iler, The chemistry of silica: solubility, polymerization, colloid and surface pro perties, and biochemistry, Wiley, 1979.
27. J. Seuring and S. Agarwal, Macromolecular rapid communications, 2012, 33, 1898-1920.
28. Y. Zhang, S. Furyk, D. E. Bergbreiter and P. S. Cremer, Journal of the American Chemical Society, 2005, 127, 14505-14510.
29. M. Ramiasa, K. Locock, C. Abrahamsson and M. Nyden, International Conference on Nanoscience and Nanotechnology (ICONN) 2014, 50-53.
30. R. Pelton, Advances in Colloid and Interface Science, 2000, 85, 1-33.
31. T. Missana and A. Adell, Journal of Colloid and Interface Science, 2000, 230, 150-156.
32. A. S. Zackrisson, J. S. Pedersen and J. Bergenholtz, Colloids and Surfaces A: Physicochemical and Engineering Aspects, 2008, 315, 23-30.
33. T. Witten and P. Pincus, Macromolecules, 1986, 19, 2509-2513.
34. B. Binks and S. Lumsdon, Langmuir, 2001, 17, 4540-4547.
35. D. Bonn, H. Kellay, H. Tanaka, G. Wegdam and J. Meunier, Langmuir, 1999, 15, 7534-7536.
36. L. L. Hench and J. K. West, Chemical Reviews, 1990, 90, 33-72.
37. G. Q. Lu, X. S. Zhao and T. K. Wei, Nanoporous materials: science and engineering, Imperial College Press, 2004.
38. M. Evans and F. Heller, Environmental magnetism: principles and applications of enviromagnetics, Academic press, 2003.
39. R. F. Butler, Paleomagnetism: magnetic domains to geologic terranes, Blackwell Scientific Publications Boston, 1992.
40. T. Kimura, M. Yamato, W. Koshimizu, M. Koike and T. Kawai, Langmuir, 2000, 16, 858-861.
41. K. Aurich, S. Nagel, G. Glöckl and W. Weitschies, Analytical Chemistry, 2007, 79, 580-586.
42. K. Heister, T. J. Keijzer and J. G. Loch, Soil Science, 2004, 169, 632-639.
43. G. Mesri, Clays and Clay Minerals, 1971, 19, 151-158.
44. D. M. Eitzman, R. Melkote and E. Cussler, AIChE Journal, 1996, 42, 2-9.

45. P. Porion, S. Rodts, M. Al-Mukhtar, A.-M. Faugère and A. Delville, Physical Review Letters, 2001, 87, 208302.
46. J. P. DeRocher, B. T. Gettelfinger, J. Wang, E. E. Nuxoll and E. Cussler, Journal of Membrane Science, 2005, 254, 21-30.
47. Y. Huang, M. Lee, M. Yang and C. Chen, Applied Clay Science, 2010, 49, 163-169.
48. S. Babu, J. C. Gimel and T. Nicolai, The Journal of Physical Chemistry B, 2008, 112, 743-748.
49. R. Nave, Hyperphysics project, [Accessed on: 1 June], http://hyperphysics.phy-astr.gsu.edu/hbase/HPhc.html.
50. T. D. Claridge, High-resolution NMR techniques in organic chemistry, Newnes, 2008.
51. M. Young, P. Carroad and R. Bell, Biotechnology and Bioengineering, 1980, 22, 947-955.
52. R. Leary, P. A. Midgley and J. M. Thomas, Accounts of Chemical Research, 2012, 45, 1782-1791.
53. M. MacGregor-Ramiasa, C. Abrahamsson, M. Röding and M. Nydén, Applied Clay Science, 2015 Submitted.
54. L. J. Michot, C. Baravian, I. Bihannic, S. Maddi, C. Moyne, J. F. Duval, P. Levitz and P. Davidson, Langmuir, 2008, 25, 127-139.
55. D. Kleshchanok, V. Meester, C. E. Pompe, J. Hilhorst and H. N. Lekkerkerker, The Journal of Physical Chemistry B, 2012, 116, 9532-9539.
56. N.-S. Cheng, Industrial & Engineering Chemistry Research, 2008, 47, 3285-3288.
57. R. Behrends, K. Fuchs, U. Kaatze, Y. Hayashi and Y. Feldman, The Journal of Chemical Physics, 2006, 124, 144512.
58. Patent, US8071509 B2, 2011.
59. P. Porion, A. M. Faugère, L. J. Michot, E. Paineau and A. Delville, The Journal of Physical Chemistry C, 2011, 115, 14253-14263.
60. A. A. Verhoeff, R. P. Brand and H. Lekkerkerker, Molecular Physics, 2011, 109, 1363-1371.
61. A. L. op Reinink, E. van den Pol, A. Petukhov, G. Vroege and H. Lekkerkerker, The European Physical Journal Special Topics, 2013, 222, 3053-3069.
62. D. van der Beek, A. Petukhov, P. Davidson, J. Ferre, J. Jamet, H. Wensink, G. Vroege, W. Bras and H. Lekkerkerker, Physical Review E, 2006, 73, 041402.
63. J. Tang and S. Fraden, Physical Review Letters, 1993, 71, 3509.
64. C. Abrahamsson, L. Nordstierna, M. Nordin, S. V. Dvinskikh and M. Nydén, Journal of Colloid and Interface Science, 2015, 437, 205-210.

65. T. Hoare, B. P. Timko, J. Santamaria, G. F. Goya, S. Irusta, S. Lau, C. F. Stefanescu, D. Lin, R. Langer and D. S. Kohane, Nano Letters, 2011, 11, 1395-1400.
66. K. Zhang and X. Y. Wu, Biomaterials, 2004, 25, 5281-5291.
67. D. Oulkadi, M. Yemloul, S. Desobry-Banon and D. Canet, Microporous and Mesoporous Materials, 2013, 172, 213-216.
68. A. Suzuki and M. Yoshikawa, The Journal of Chemical Physics, 2006, 125, 174901.
69. M. Kolb, R. Botet and R. Jullien, Physical Review Letters, 1983, 51, 1123.
70. D. Weitz, J. Huang, M. Lin and J. Sung, Physical Review Letters, 1985, 54, 1416.
71. G. Dietler, C. Aubert, D. S. Cannell and P. Wiltzius, Physical Review Letters, 1986, 57, 3117.
72. P. Xu and B. Yu, Advances in Water Resources, 2008, 31, 74-81.
73. C. H. Blomqvist, C. Abrahamsson, T. Gebäck, A. Altskär, A.-M. Hermansson, M. Nydén, S. Gustafsson, N. Lorén and E. Olsson, Colloids and Surfaces A: Physicochemical and Engineering Aspects, doi:10.1016/j.colsurfa.2015.07.032 In press
74. M. R. Noll, C. Bartlett and T. M. Dochat, Proceeding of the Sixth National Outdoor Action Conference on Aquifer Restoration, Ground Water Monitoring, and Geophysical Method, National Ground Water Association, 1992.
75. M. C. Harvey and S. D. Stearns, Journal of Chromatographic Science, 1983, 21, 473-477.
76. C. Yu, S. Mutlu, P. Selvaganapathy, C. H. Mastrangelo, F. Svec and J. M. Fréchet, Analytical Chemistry, 2003, 75, 1958-1961.
77. R. Ciriminna, A. Fidalgo, V. Pandarus, F. o. Béland, L. M. Ilharco and M. Pagliaro, Chemical Reviews, 2013, 113, 6592-6620.
78. T. Hoare and R. Pelton, Macromolecules, 2004, 37, 2544-2550.
79. V. Lapeyre, I. Gosse, S. Chevreux and V. Ravaine, Biomacromolecules, 2006, 7, 3356-3363.